

A study of the MAD accretion state across black hole spins for radiatively inefficient accretion flows.

G.-Q. ZHANG ^{1,2} DAMIEN BÉGUÉ ² A. PE'ER ² AND B.-B. ZHANG ^{1,3}

¹*School of Astronomy and Space Science, Nanjing University, Nanjing 210093, China*

²*Bar Ilan University, Ramat Gan, Israel*

³*Key Laboratory of Modern Astronomy and Astrophysics (Nanjing University), Ministry of Education, China*

ABSTRACT

The study of Magnetically Arrested Disks (MAD) attract strong interest in recent years, as these disk configurations were found to generate strong jets as observed in many accreting systems. Here, we present the results of 14 general relativistic magnetohydrodynamic (GRMHD) simulations of advection dominated accretion flow in the MAD state across black hole spins, carried with cuHARM. Our main findings are as follows. (i) The jets transport a significant amount of angular momentum to infinity in the form of Maxwell stresses. For positive, high spin, the rate of angular momentum transport is about 5 times larger than for negative spin. This contribution is nearly absent for a non-rotating black hole. (ii) The mass accretion rate and the MAD parameter, both calculated at the horizon, are not correlated. However, their time derivatives are anti-correlated for every spin. (iii) For zero spin, the contribution of the toroidal component of the magnetic field to the magnetic pressure is negligible, while for fast spinning black hole, it is in the same order as the contribution of the radial magnetic component. For high positive spin, the toroidal component even dominates. (iv) For negative spins, the jets are narrower than their positive spin counterparts, while their fluctuations are larger. The weak jet from the non-rotating black hole is the widest with the smallest fluctuations. Our results highlight the complex, non-linear connection between the black hole spin and the resulting disk and jet properties in the MAD regime.

Keywords: Accretion – Magnetohydrodynamics – Black hole physics – Computational methods

1. INTRODUCTION

Accretion disks are ubiquitous in many astronomical objects, such as active galactic nuclei (AGNs) and X-ray binaries. The structure of the accretion disk mainly depends on the accretion rate. At high accretion rate, close to the Eddington limit, the disks are typically geometrically thin and optically thick, and the models from Novikov & Thorne (1973) and Shakura & Sunyaev (1973) are thought to accurately describe their physics. When the accretion rate is much lower than the Eddington accretion rate, the cooling time becomes longer than the accretion time, leading to a radiatively inefficient accretion flow (RIAF), and the disk becomes geometrically thick and optically thin. In this regime, there are several theoretical disk models, such as the Advection-dominated accretion flow (ADAF, Narayan & Yi 1994, 1995; Abramowicz et al. 1995; Yuan & Narayan 2014). The estimated low luminosity of Sagittarius A* as well as the black hole at the center of the M87 galaxy compared to the Eddington luminosity suggests that these black holes accrete in the form of an ADAFs (Yuan et al. 2002).

It is widely believed that the structure of an accretion flow consists of a turbulent accretion disk, a bipolar jet and a magnetized wind (see e.g. McKinney & Gammie 2004; De Villiers et al. 2003). The details of this structure strongly depend on the configuration and the strength of the magnetic field inside and outside the disk. The magnetic fields in the disk, either advected from large distances or created in situ by the dynamo effect, are amplified by the magnetorotational instability (MRI, Balbus & Hawley 1991a, 1998a). They ultimately drive angular momentum transport, regulate accretion and produce a bipolar, strongly magnetized jet. There are two distinct modes of accretion, depending on the magnetic fields surrounding the black hole, which ultimately lead to two different disk configurations. In the Standard And Normal Evolution (hereinafter SANE, Narayan et al. 2012; Sądowski et al. 2013), the magnetic field pressure is not strong and the accretion process is smooth. The accretion disk, although turbulent, extends nearly

evenly up to the horizon. In this accretion mode, angular momentum is transported mostly radially inside the disk by MRI (Chatterjee & Narayan 2022).

The second type of disk is termed Magnetically Arrested Disk (MAD, Bisnovatyi-Kogan & Ruzmaikin 1974; Narayan et al. 2003a; Igumenshchev 2008). In this model, the magnetic flux accumulates near the horizon until it saturates. In fact, the accumulated magnetic field becomes so strong close to the black hole that it can change the dynamics of the in-falling matter, thereby regulating the accretion. It was found in 2D simulations that the accretion can be nearly fully stopped by the magnetic pressure, and then resumes following the reconnection of the magnetic field lines at the equator (see, e.g. Chashkina et al. 2021). This picture however only partially holds in 3D simulations: accretion continuously proceeds, via the development of non-axisymmetric instabilities (Sruuit et al. 1995; Begelman et al. 2022), with the in-falling gas being shaped into filaments by the strong magnetic field (see e.g. Figure 1 of Xie & Zdziarski (2019), and Wong et al. (2021)).

The MAD state attracted increasingly more attention in the past few years, following the observation of the closest region to the super-massive black hole in M87 and Sagittarius A* by the Event Horizon Telescope (EHT) collaboration (Event Horizon Telescope Collaboration et al. 2019, 2022a). By comparing the images taken in the radio band to post-processed GRMHD simulations, it was determined that the accretion should operate in the MAD state for those two black holes (Event Horizon Telescope Collaboration et al. 2021, 2022b). Yuan et al. (2022) independently arrived at the same conclusion for M87 by studying rotation measurements. Moreover, several studies, including Dexter et al. (2020a); Porth et al. (2021a); Ripperda et al. (2022); Scepi et al. (2022), proposed a model in which the flares observed in Sagittarius A* by the GRAVITY experiment (GRAVITY Collaboration et al. 2018, 2020) have their origin in the magnetic flux eruptions, characteristics of the MAD state (Igumenshchev 2008). It is clear that the MAD state is ubiquitous at low accretion rate, and better understanding its properties will shed light on key observations of black holes and their physics.

An important characteristics of the MAD state is the saturated magnetic flux at the horizon. Since numerical studies of disk evolution depend on assumed initial conditions, in order to numerically study these systems one has to use an appropriate initial magnetic field configuration. Tchekhovskoy et al. (2011) found such a configuration that results in the transport of a large amount of magnetic flux to the horizon. Using normalized black hole spin parameter $a = 0.99$, they found that the disk would be in the MAD state when the MAD parameter reaches $\Phi_B \sim 50$. Here and below, the MAD parameter is defined as the ratio of the magnetic flux to the square root of the mass accretion rate at the horizon. Later, Tchekhovskoy & McKinney (2012) performed two simulations with $a = 0.9$ and $a = -0.9$ and found that the MAD parameter of the retrograde disk is about 30, smaller than that of prograde disk. Narayan et al. (2022) studied the dependence on the spin of the MAD parameter, confirmed the results from Tchekhovskoy & McKinney (2012) and also found that the maximal value of the MAD parameter (for a given initial magnetic configuration) is, in fact, reached for a black hole spin $a \simeq 0.5$.

The MAD parameter Φ_B is an important quantity in quantifying both the disk structure and the emerging jet. It was found that disks in the MAD state around rotating black holes launch strong and powerful jets via the Blandford & Znajek (1977) mechanism (see e.g. Tchekhovskoy et al. 2011). The emerging power of the magnetized jet is proportional to the square of the MAD parameter multiplied by the mass accretion rate (Tchekhovskoy et al. 2011). It is therefore important to constrain the accretion parameters and mechanisms which determine and regulate the value and the duty cycle of the MAD parameter.

The strong magnetic field during the MAD state pushes out the gas and stops, or at least regulates the dynamics of the in-falling of matter. Therefore, one may naively expect that an increase of the magnetic flux should result in the decrease of the mass accretion rate, namely, that they are anti-correlated. An anti-correlation is also expected if accretion proceeds by interchange instability, as matter replaces a highly magnetized region closer to the black hole resulting in a drop in the MAD parameter (Porth et al. 2021a). However, Porth et al. (2021a) did not find a correlation or an anti-correlation between the mass accretion rate \dot{M} and Φ_B . Here, we expand their results for all black hole spins: as we show below, none of our simulations show a correlation or an anti-correlation between \dot{M} and Φ_B . On the other hand, we do find an anti-correlation between their time derivatives.

A complete understanding of the interplay between accretion and saturated magnetic field close to the horizon and how it impacts the structure and power of the disk, jet and wind, as well as their evolution is still missing. Narayan et al. (2022) found that prograde disks have wider jets and that the shape itself depends on the spin of the black hole. The structure of the jet and the disk mainly depends on the magnetic field pressure and the gas pressure inside the disks and jets. Begelman et al. (2022), using the simulation in the MAD regime around a rotating BH with $a = 0.9375$

from Dexter et al. (2020b,a), proposed that the disk properties in this regime are due to a dynamically important toroidal field in the close vicinity of the black hole. However, Chatterjee & Narayan (2022) studying accretion in the case of a non-rotating black hole, showed that the radial magnetic field b^r is actually stronger than the toroidal magnetic field at small radii. This apparent inconsistency needs to be resolved, even though its origin, namely the black hole spin, is trivially identified. Here, we find that, close to the BH horizon, the toroidal component of the magnetic field, b^ϕ is increasing with the absolute value of the BH spin, $|a|$, being dynamically unimportant for $a = 0$, but dominant for $|a| \rightarrow 1$.

It is generally thought that the strong magnetic field close to the black hole suppresses the development of MRI, as the disk height is smaller than the wavelength of the most unstable vertical mode (McKinney et al. 2012; Marshall et al. 2018; White et al. 2019). This, in turn, affects the rate of angular momentum transport inside the disk, which details are still poorly understood in the MAD state. Recently, Begelman et al. (2022) argued that MRI is actually not suppressed closest to the black-hole by considering non-axisymmetric modes (Das et al. 2018). On the other hand, Chatterjee & Narayan (2022) demonstrated that a for non-rotating black hole, angular momentum is transported predominantly by magnetic flux eruptions, characteristics of a disk in the MAD state. It remains to understand if the contribution of this process still dominates the transport of angular momentum over MRI in the case of a rotating black hole. In addition, angular momentum from the disk is transported by the emerging winds above and below it.

An additional source of angular momentum from an accretion disk system is the jet, in the form of Maxwell stresses. This contribution to the angular momentum originates mainly from the black hole, rather than the disk, and as such acts to spin down the black hole (Chatterjee & Narayan 2022). As we show here, this transport can significantly contribute to the amount of angular momentum deposited to the external medium. Since the power of the jet depends on the BH spin, this also constrains the cosmic period over which the system is active. The net rate of angular momentum has a strong dependence on the spin and is the largest for prograde disks.

The shape of the jet itself also depends on the BH spin. It is determined by the balance between the internal and external stresses. As explained above, the main source of stresses are the magnetic field components, which, in turn depend on the BH spin. Furthermore, the BH spin not only affects the time-average jet shape, but also fluctuations around it. As we show here, retrograde disks produce the narrowest jets with the largest fluctuations, while non-spinning BHs produce the widest jets with the narrowest fluctuations.

Given the complexity of accreting systems, many previous works used general relativistic (eventually radiative and two temperatures) magnetohydrodynamic (GRMHD) simulations to investigate the properties and evolutionary process of MAD disks (Narayan et al. 2012; Sądowski et al. 2013; Porth et al. 2017; White et al. 2020; Porth et al. 2021b; Begelman et al. 2022; Narayan et al. 2022; Chatterjee & Narayan 2022). In the past two decades, with the rapid increase in compute capability, these simulations have become increasingly popular and practical (Gammie et al. 2003; Anninos et al. 2005; Stone et al. 2008; Noble et al. 2006; Porth et al. 2017; Tekehovskoy 2019; Liska et al. 2022; Bégué et al. 2023). In addition, general-purpose graphics processing units (GPU) started to be used to accelerate fluid simulations in recent years, as they are particularly well-suited to be ran on GPUs. As a result, several GRMHD codes can now use GPU accelerators, see e.g. Chandra et al. (2017); Liska et al. (2020); Bégué et al. (2023); Shankar et al. (2022). *grim* uses the library ArrowFire to achieve GPU compatibility (Chandra et al. 2017). Liska et al. (2020) developed H-AMR with openMP, MPI and CUDA. Building on HARMPI, our group developed a new GPU-accelerated GRMHD code, cuHARM, which uses openMP and cuda (Bégué et al. 2023). This code is thoroughly optimized for maximal harness of the power available in NVidia GPUs, with more than 50% computation efficiency on NVidia A100 cards. For the results presented here, the simulations are made on a single multi-GPU workstation.

In this paper, using our GRMHD code cuHARM, we study the role played by the magnetic field in the MAD state for different black hole spins, and its effect on the structure of the disk and the jet. For this, we present several simulations with different initial magnetic field strengths and black hole spins. This paper is organized as follows. In Section 2, we present the setup of our simulations and introduce the numerical diagnostics used in our analysis. We discuss the dynamics of the accretion disk system in our simulations in Section 3. In particular, after specifying the inflow and outflow equilibrium radius and the time evolution of \dot{M} and ϕ_B in section 3.1 and 3.2 respectively, we study (i) the absence of correlation between the mass accretion rate and the MAD parameter, and introduce the anti-correlation between their time derivative in section 3.3; (ii) the shape of the jet as a function of spin in section 3.7, finding that the retro-grade disks are narrower than their corresponding prograde disks; and (iii) the component-wise contributions of the magnetic pressure to underline the differences between a spinning and a non-spinning black-hole in section 3.8, where the toroidal component is found to be sub-dominant for $a = 0$ but similar to the radial component for large

|a|. In section 4, we discuss the transport of angular momentum for our simulations with spin $a = -0.94$, $a = 0$ and $a = 0.94$, underlying the differences between each black hole spins. The summary and conclusions of the paper are given in Section 5.

2. SIMULATIONS

We perform several simulations with cuHARM (Bégué et al. 2023), which uses the finite volume method to numerically solve the conservative GRMHD equations (for reviews, see *e.g.* Martí & Müller 2003; Font 2008; Rezzolla & Zanotti 2013). The code is written in CUDA-C and openMP, and all calculations of cuHARM are accelerated by GPU (only the data transfer and exports are powered by CPU). To perform the simulations which results are presented in this article, we use an Nvidia DGX-V100 server with 8 Nvidia V100 GPUs .

2.1. Initial setup

In this paper, we study on the accretion flows in the MAD state around a spinning black hole. Our simulations begin with the stationary axisymmetric torus described by Fishbone & Moncrief (1976). We set the gas adiabatic index to $\Gamma = 14/9$, and consider an initially large disk with $r_{\text{in}} = 20r_g$ and $r_{\text{max}} = 41r_g$, where r_{in} is the inner boundary of the disk, r_{max} is the radius at which the pressure reaches its maximum, and r_g is the gravitational radius. The matter and internal energy densities are normalized such that, for the initial disk, the maximum matter density ρ in the entire disk is normalized to $\rho_{\text{max}} = 1$. The internal energy density is scaled accordingly. Since the initial torus is in equilibrium, it does not spontaneously evolve. We therefore add small random perturbations (set to 4%) to the internal energy density u as the seed of instabilities, which will promote accretion.

This initial torus is in full hydrodynamic equilibrium and, as such, it does not contain any magnetic field. We introduce a purely poloidal subdominant magnetic field defined by the vector potential \mathbf{A} , such that $A_r = A_\theta = 0$ and

$$A_\phi = \max \left[0, \left(\frac{\rho}{\rho_{\text{max}}} \right) \left(\frac{r}{r_{\text{in}}} \sin \theta \right)^3 \exp \left(-\frac{r}{400} \right) - 0.2 \right], \quad (1)$$

which has been previously employed in, *e.g.*, Wong et al. (2021); Narayan et al. (2022). Here r , θ and ϕ are the horizon penetrating spherical Kerr-Schild coordinates. The corresponding magnetic field is initially a single loop confined to the disk. The magnitude of the magnetic field is further normalised by the parameter $\beta_0 = p_{\text{gas,max}}/p_{\text{b,max}} \gg 1$, where $p_{\text{gas,max}}$ is the maximum gas pressure, $p_{\text{b,max}} = b^2/2$ is the maximum of the magnetic field pressure, and $b = b^\mu b_\mu$ is the norm of the 4-vector magnetic field, see Section 2.3 below. This expression of the magnetic field is designed to ensure that enough magnetic flux can be transported to the black hole throughout the course of the simulation and "saturates" its magnetosphere; see further discussion in Tchekhovskoy et al. (2011).

We conduct a series of simulations with different black hole spins, $a \in \{-0.985, -0.94, -0.85, -0.5, 0, 0.5, 0.85, 0.94, 0.985\}$ and an initial magnetization $\beta_0 = 100$. In the case of the retrograde disk with $a = -0.94$, we also varied the initial magnetic field strengths, with $\beta_0 \in \{100, 200, 400, 800\}$. We evolve most of the simulations until $t = 2 \times 10^4 t_g$, where $t_g = r_g/c$, apart for aM94b800, which is evolved to $t = 2.5 \times 10^4 t_g$ due to the weak initial magnetic field and the longer time required to reach the MAD state for this setup. Additionally, simulation aM94b100h is evolved until $t = 5 \times 10^4 t_g$ in order to study the long time behavior of our accretion disk system. We use the spin and the initial β_0 to name the simulations: "a" stands for spin, "M" indicates a negative value, and "b" represents the initial β_0 , such that, for instance, aM94b100 stands for a simulation with the negative ("M") spin $a = -0.94$ and an initial $\beta_0 = 100$. A summary of all the simulations used in this work is given in Table 1.

2.2. Numerical aspects

Since we are studying accretion around rotating black hole, we use the Kerr metric for our simulations. The Kerr-Schild (KS) coordinate system (t, r, θ, ϕ) is used as the physical coordinates, while to both enhance the robustness of the calculation and focus the computation in the region of interest, namely close to the black hole and at the equator, the modified Kerr-Schild (MKS, see *e.g.* McKinney & Gammie 2004) coordinates (t, q^1, q^2, ϕ) are used in the numerical calculation. The relation between these coordinates, as implemented in cuHARM, can be found in section 4.1 of Bégué et al. (2023).

We use the inflow and outflow boundary conditions in the radial direction at small and large radii, respectively. In the θ direction we use the reflective boundary condition, and the periodic boundary condition is used in the ϕ direction.

Name	β_0	spin	Resolution $N_r \times N_\theta \times N_\phi$	MAD parameter	Accretion Rate	Jet Efficiency
aM985b100	100	-0.985	$192 \times 96 \times 96$	$12.26^{+2.58}_{-2.02}$	$23.54^{+9.54}_{-6.52}$	$0.28^{+0.15}_{-0.11}$
aM94b100	100	-0.94	$192 \times 96 \times 96$	$14.46^{+3.99}_{-2.23}$	$24.30^{+10.19}_{-8.60}$	$0.26^{+0.15}_{-0.09}$
aM85b100	100	-0.85	$192 \times 96 \times 96$	$17.59^{+3.52}_{-2.97}$	$22.62^{+10.76}_{-6.55}$	$0.26^{+0.12}_{-0.10}$
aM5b100	100	-0.5	$192 \times 96 \times 96$	$26.24^{+2.28}_{-3.34}$	$31.55^{+9.58}_{-9.15}$	$0.11^{+0.02}_{-0.02}$
a0b100	100	0	$192 \times 96 \times 96$	$30.94^{+2.25}_{-5.08}$	$15.12^{+2.44}_{-2.46}$	$0.06^{+0.01}_{-0.01}$
a5b100	100	0.5	$192 \times 96 \times 96$	$32.73^{+7.02}_{-6.56}$	$45.16^{+15.28}_{-12.90}$	$0.22^{+0.07}_{-0.06}$
a85b100	100	0.85	$192 \times 96 \times 96$	$29.94^{+5.10}_{-4.79}$	$34.23^{+14.34}_{-11.36}$	$0.90^{+0.29}_{-0.25}$
a94b100	100	0.94	$192 \times 96 \times 96$	$25.37^{+4.27}_{-4.20}$	$32.15^{+13.39}_{-10.26}$	$1.05^{+0.36}_{-0.38}$
a985b100	100	0.985	$192 \times 96 \times 96$	$22.69^{+3.93}_{-3.69}$	$32.63^{+15.74}_{-10.80}$	$1.22^{+0.47}_{-0.32}$
aM94b200	200	-0.94	$192 \times 96 \times 96$	$15.09^{+2.66}_{-2.89}$	$20.75^{+6.46}_{-6.04}$	$0.28^{+0.12}_{-0.11}$
aM94b400	400	-0.94	$192 \times 96 \times 96$	$16.37^{+2.40}_{-2.21}$	$20.41^{+5.85}_{-4.92}$	$0.34^{+0.10}_{-0.08}$
aM94b800	800	-0.94	$192 \times 96 \times 96$	$16.22^{+1.80}_{-1.67}$	$15.36^{+5.78}_{-4.60}$	$0.33^{+0.07}_{-0.06}$
a0b100h	100	0	$256 \times 128 \times 128$	$32.84^{+4.23}_{-4.10}$	$43.12^{+17.25}_{-11.14}$	$0.07^{+0.01}_{-0.01}$
aM94b100h	100	-0.94	$256 \times 128 \times 128$	$15.13^{+1.81}_{-3.18}$	$23.94^{+10.65}_{-8.57}$	$0.27^{+0.07}_{-0.12}$

Table 1. List of the simulations presented in this paper with their initial magnetization β_0 , spin a and resolution. The three last columns give the time-average value of the MAD parameter Φ_B , of the accretion rate \dot{M} and of the jet efficiency η for $10^4 t_g < t < 2 \times 10^4 t_g$ ($1.5 \times 10^4 t_g < t < 2.5 \times 10^4 t_g$ for aM94b800, $10^4 t_g < t < 5 \times 10^4 t_g$ for aM94b100h).

To address the potential numerical errors in empty or strongly magnetized region, we adopt the same flooring model as in Bégué et al. (2023), which is used in many other papers, e.g. Porth et al. (2019). The density ρ and the internal energy u are limited using

$$\rho = \max\left(\rho, 10^{-20}, 10^{-5} r^{-\frac{3}{2}}\right), \quad (2)$$

$$u = \max\left(u, 10^{-20}, \frac{10^{-5}}{3} r^{-\frac{5}{2}}\right). \quad (3)$$

Matter and energy are added when needed to preserve the conditions $b^2/\rho < 50$ and $b^2/u < 2.5 \times 10^3$.

The reference resolution of most simulations is $(N_r \times N_\theta \times N_\phi) = (192, 96, 96)$, except for aM94b100h and a0b100h, which have a slightly higher resolution $(N_r \times N_\theta \times N_\phi) = (256, 128, 128)$. Here, the "h" appended to the name stands for "high resolution". The resolution of the simulations presented in this paper is somewhat lower than that used in some of the simulations presented in recent works. For example, Narayan et al. (2022) performed fairly similar simulations with a resolution of $288 \times 192 \times 144$. White et al. (2020) examined the impact of different resolutions, and they argued that the accretion rate and the general disk structure agree across the simulations with different resolution. We use our higher resolution simulations, aM94b100h and a0b100h, to check the solidity of our results to a change in the resolution. We did not find any significant difference between the low and high resolution simulations.

2.3. Diagnostics

Following Komissarov (1999), let $b^\mu \equiv (\star F)^{\mu\nu} u_\nu$ represent the 4-vector magnetic field and u^μ be the 4-velocity, which is orthogonal to b^μ . In the ideal MHD limit, the dual to the Faraday tensor is given by

$$(\star F)^{\mu\nu} = b^\mu u^\nu - b^\nu u^\mu. \quad (4)$$

In this limit of a perfect magnetized fluid, the stress energy tensor $T^{\mu\nu}$ is given by

$$T^{\mu\nu} = (h + b^2) u^\mu u^\nu + \left(p_g + \frac{b^2}{2}\right) g^{\mu\nu} - b^\mu b^\nu. \quad (5)$$

Here, $h = \rho + u + p_g$ is the enthalpy, p_g is the gas pressure, $b^2 = b^\mu b_\mu$ and $g^{\mu\nu}$ is the metric tensor with determinant noted $\sqrt{-g}$. Using cuHARM, we solve the general relativistic magneto-hydrodynamic equations, namely

$$\nabla_\mu (\rho u^\mu) = 0 \quad (6)$$

$$\nabla_{\mu}(T^{\mu\nu}) = 0 \quad (7)$$

$$\nabla_{\mu}(\star F^{\mu\nu}) = 0 \quad (8)$$

which respectively are the equations of mass conservation, the equation of energy and momentum conservation, and the homogeneous Maxwell's equations.

The MAD state mainly depends on the magnetic flux through the horizon, Therefore, we define the following radial diagnostics, which can eventually be evaluated at the horizon:

1. The mass accretion rate:

$$\dot{M}(r) = \int_{\theta=0}^{\theta=\pi} \int_{\phi=0}^{\phi=2\pi} \sqrt{-g} \rho u^r d\theta d\phi. \quad (9)$$

2. The magnetic flux crossing the horizon (through one hemisphere):

$$\phi_B(r = r_H) = \frac{1}{2} \int_{\theta=0}^{\theta=\pi} \int_{\phi=0}^{\phi=2\pi} \sqrt{-g} |\star F^{rt}| d\theta d\phi. \quad (10)$$

3. The energy flux through the horizon towards the black hole:

$$\dot{E}(r) = - \int_{\theta=0}^{\theta=\pi} \int_{\phi=0}^{\phi=2\pi} \sqrt{-g} T^r{}_i d\theta d\phi. \quad (11)$$

4. The angular momentum flux in the radial direction:

$$\dot{J}_r(r) = \int_{\theta=0}^{\theta=\pi} \int_{\phi=0}^{\phi=2\pi} \sqrt{-g} T^r{}_{\phi} d\theta d\phi. \quad (12)$$

5. The MAD parameter:

$$\Phi_B = \frac{\phi_B}{\sqrt{\dot{M}(r = r_H)}} \quad (13)$$

6. The jet efficiency at the horizon:

$$\eta(r = r_H) = 1 + \frac{\dot{E}(r = r_H)}{\dot{M}(r = r_H)}. \quad (14)$$

Note that our definition of angular momentum flux \dot{J} and energy flux \dot{E} are opposite to those employed by [Narayan et al. \(2022\)](#), but are in agreement with the definitions of *e.g.* [Porth et al. \(2019\)](#). We are also interested in the structure of the disk and of the jet. Therefore, we define the additional following diagnostics.

1. The disk height, denoted by (h/r) :

$$(h/r)(t, r) = \frac{\int_0^{2\pi} \int_0^{\pi} |\frac{\pi}{2} - \theta| \rho \sqrt{-g} d\theta d\phi}{\int_0^{2\pi} \int_0^{\pi} \rho \sqrt{-g} d\theta d\phi}. \quad (15)$$

2. The ϕ -average of a quantity q :

$$\langle q \rangle_{\phi}(t, r, \theta) = \frac{\int_0^{2\pi} q \sqrt{-g} d\phi}{\int_0^{2\pi} \sqrt{-g} d\phi}. \quad (16)$$

3. The disk-average of a quantity q :

$$\langle q \rangle_{\theta, \phi}(t, r) = \frac{\int_0^{2\pi} \int_0^{\pi} q \rho \sqrt{-g} d\theta d\phi}{\int_0^{2\pi} \int_0^{\pi} \rho \sqrt{-g} d\theta d\phi}. \quad (17)$$

4. The disk-average of a quantity q but within a narrow θ range (used below in calculating the pressure):

$$\langle q \rangle_{\theta, \phi}(t, r) = \frac{\int_0^{2\pi} \int_{\theta=\pi/8}^{\theta=7\pi/8} q \rho \sqrt{-g} d\theta d\phi}{\int_0^{2\pi} \int_{\theta=\pi/8}^{\theta=7\pi/8} \rho \sqrt{-g} d\theta d\phi}. \quad (18)$$

We will also present time-averaged quantities and time- and ϕ -averaged maps, which are computed for $10^4 t_g < t < 2 \times 10^4 t_g$, unless specified otherwise, and the full 2π range for ϕ .

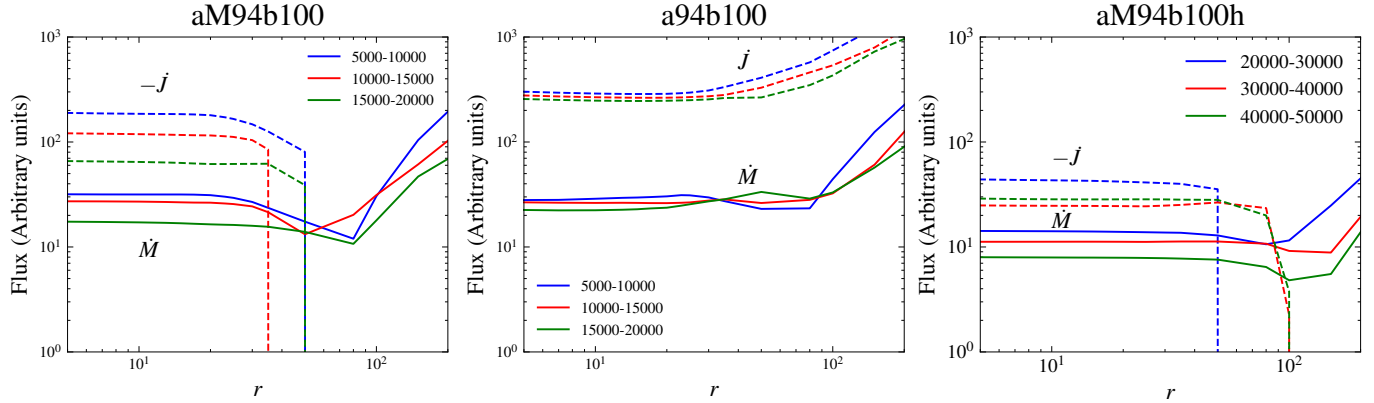


Figure 1. The radial profile of the mass accretion rate \dot{M} (solid line) and of the angular momentum flux \dot{J} (dashed line) for aM94b100 (left panel), a94b100 (middle panel) and for the long term evolution aM94b100h (right panel) at different time periods (see legend). As the time increases, the steady region extends to larger radius. This suggests that aM94b100 and a94b100 have established inflow outflow equilibrium at $r < 30r_g$ for $1.5 \times 10^4 t_g < t < 2 \times 10^4 t_g$, while it is about $70r_g$ at $4 \times 10^4 < t_g < 5 \times 10^4$ for aM94b100h. For the simulations with the negative spin on the left and right panels, the angular momentum fluxes change sign at $r = 30 - 50r_g$ and $r = 50 - 100r_g$, respectively.

3. GENERAL ACCRETION DYNAMICS

3.1. Inflow equilibrium radius and radial limit of our analysis

Most simulations are evolved until $t = 2 \times 10^4 t_g$, which is sufficient for the disk to be in the MAD state. We assume this state to be established when the MAD parameter reaches its average value at late time. We find that in all cases, the averaged MAD parameter is comparable to or greater than 15, the limiting value proposed by Tchekhovskoy et al. (2011) to define the MAD state. Only aM94b800 barely reaches the MAD state at $t = 2 \times 10^4 M$ because of the initial small magnetic field normalisation. So this simulation is evolved further until $t = 2.5 \times 10^4 M$ at which time the MAD state for this initial setup is well-established.

We first study the radial profile of the mass accretion rate \dot{M} and of the angular momentum flux \dot{J} , as given by Equations (9) and (12), respectively. The results are displayed on the left and middle panel of Figure 1 for simulations aM94b100 and a94b100, serving as examples. The results are similar for all other simulations. For aM94b100 and a94b100, the radial profiles of \dot{M} and \dot{J} are averaged over 3 different time intervals, namely from 5×10^3 to $10^4 t_g$, from 10^4 to $1.5 \times 10^4 t_g$ and from 1.5×10^4 to $2 \times 10^4 t_g$. In the last time interval, the mass accretion rates of these two runs are independent of the radius r for $r < 30r_g$. The angular momentum fluxes also exhibit a similar pattern, remaining constant at $r < 30r_g$. This means that the inner region with $r < 30r_g$ is in inflow equilibrium state.

There are two key differences between the prograde and retrograde cases. Firstly, the sign of the angular momentum flux is different. The prograde black hole has a positive angular momentum flux, namely, the black hole is losing angular momentum, as was previously reported in Narayan et al. (2022). Conversely, the angular momentum flux of the retrograde black hole is negative, meaning that it accumulates positive angular momentum and spins down. The second difference is the existence of a radius at which the angular momentum flux changes sign for a retrograde black hole. This indicates that there is a net flux of angular momentum away from the black hole at large distance. This radius is also observed in the simulation presented in Narayan et al. (2022), see their figure 3 with the sharp drop of angular momentum flux at $r \sim 10^2 r_g$. We discuss in more details the differences for the angular momentum transport between prograde and retrograde disks in section 4.

The duration of most of our simulations is shorter than recent long-time simulations. For example, Narayan et al. (2022) evolved the accretion system until $t = 10^5 t_g$, such that they obtained an inflow equilibrium radius at $\sim 100r_g$, larger than ours by a factor 3 to 4. To verify the reliability of our results over a longer time span, we extend the simulation aM94b100h to $t = 5 \times 10^4 t_g$. In the right panel of Figure 1, we present the radial profile of the mass accretion rate \dot{M} and the angular momentum flux \dot{J} for this extended period. The time-averaged quantities for $2 \times 10^4 t_g < t < 3 \times 10^4 t_g$, $3 \times 10^4 t_g < t < 4 \times 10^4 t_g$ and $4 \times 10^4 t_g < t < 5 \times 10^4 t_g$ are displayed. These profiles show the same behavior as aM94b100 but the inflow equilibrium radius now extends to $r > 50r_g$. Therefore, the shorter simulation time does not affect the establishment of the equilibrium state but only limit the inflow equilibrium to

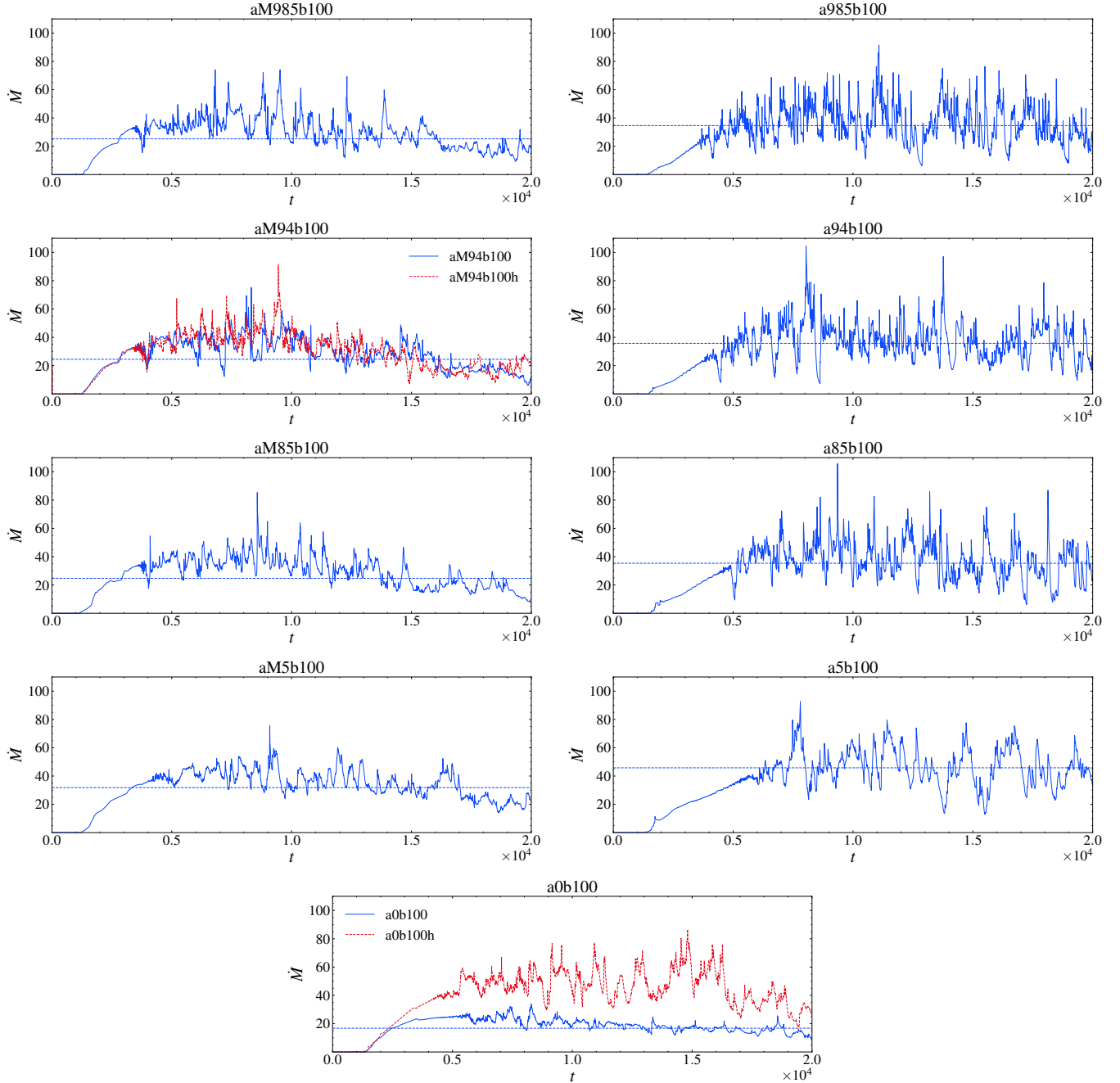


Figure 2. Time evolution of the mass accretion rate \dot{M} . The left column pertains to retrograde disks, while the right columns corresponds to prograde disks. For convenience, we set the y-axes to identical scales to facilitate direct comparison. The horizontal lines are the time-averaged mass accretion rate \dot{M} , where the averaged is taken from $10^4 t_g$ to $2 \times 10^4 t_g$.

smaller radius. In the following, we will focus on the inner region characterized by $r \leq 30_g$ and demonstrate, where relevant, that we obtain similar results to those presented in Narayan et al. (2022). Considering that we are using (i) a different numerical scheme, (ii) a different numerical resolution, and (iii) analysing the results earlier in the simulation, this shows the solidity of these results.

3.2. Mass accretion rate and magnetic flux at the horizon

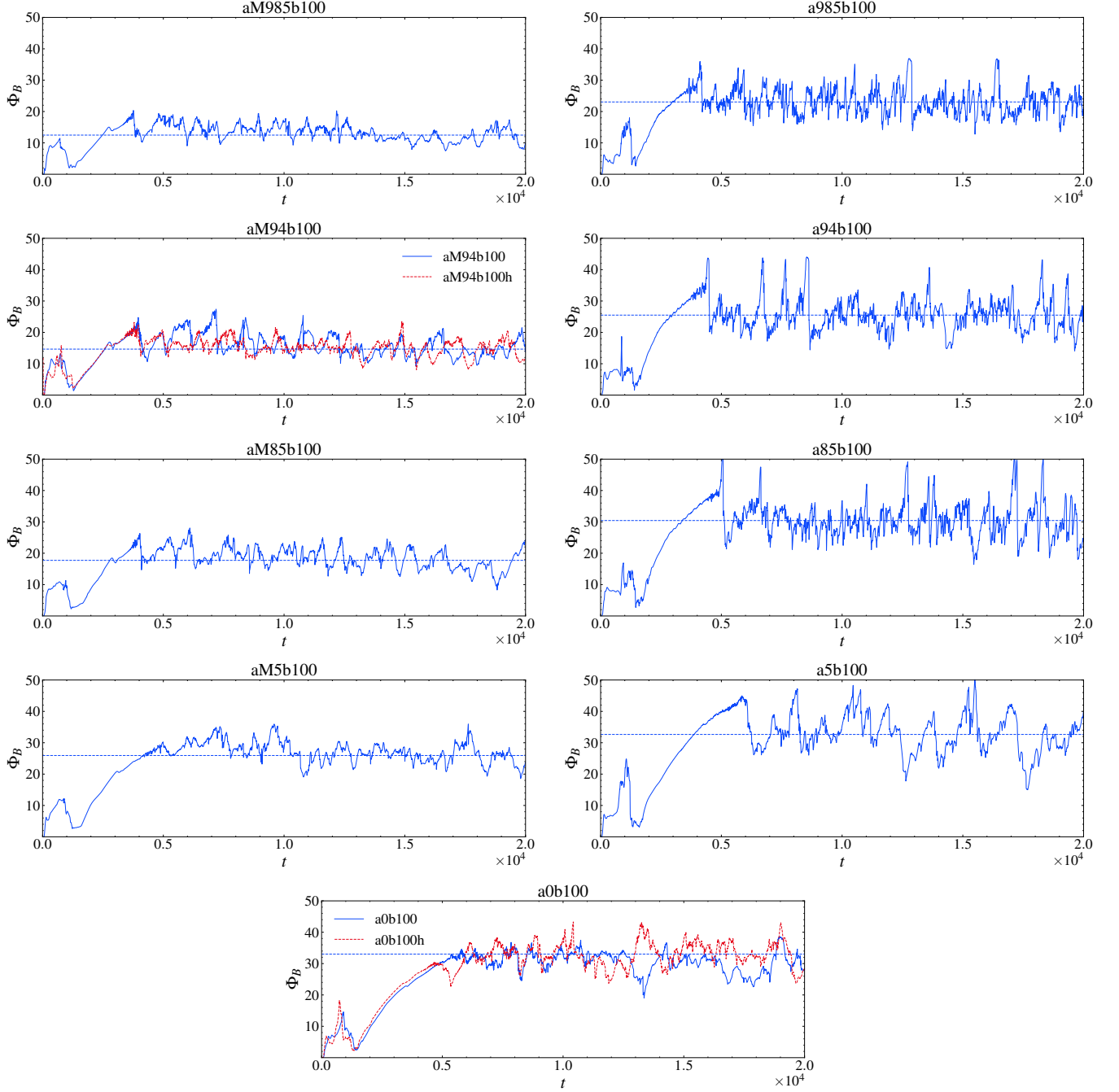


Figure 3. The time evolution of MAD parameters Φ_B . The left column represents retrograde disks, while the right column is for prograde disks. We use the horizontal lines to denote the time-averaged Φ_B from $10^4 t_g$ to $2 \times 10^4 t_g$, which is referred to as the typical MAD parameter during the MAD state.

The time evolution of the mass accretion rate \dot{M} at the horizon, derived from Equation 9, are shown in Figure 2 for all simulations with different spins. The same rough behaviour is observed in all cases. After an initial quiet period, the mass accretion rate steadily increases to reach its late time average around $t \sim 5 \times 10^3 t_g$. The left column of Figure 2 shows the time evolution of \dot{M} for retrograde disks, while the corresponding prograde disks are displayed in the right column. The y-axis scale is identical to facilitate comparison. There is a clear dependence of the mass accretion rate

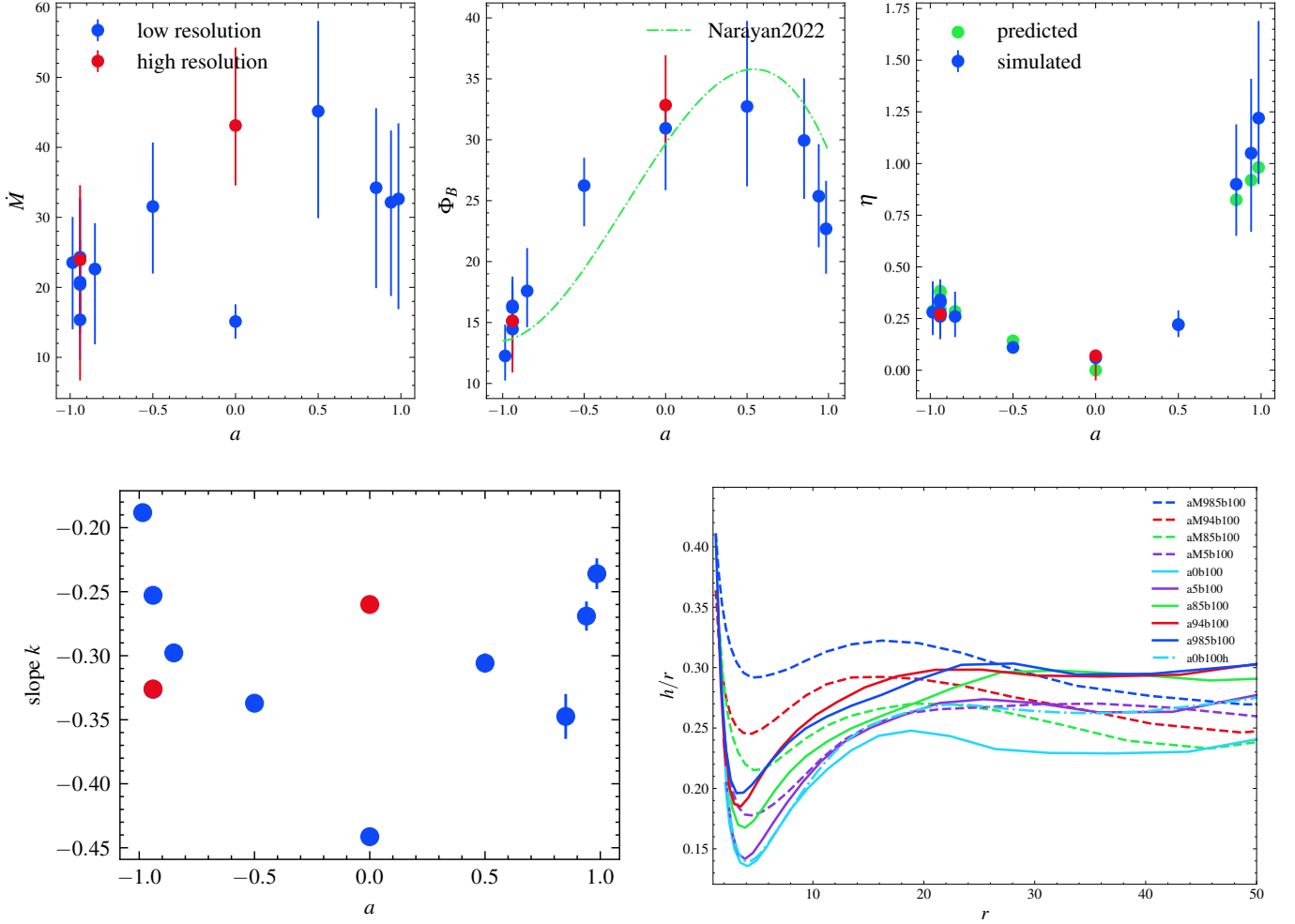


Figure 4. Spin-dependence of several disk and jet properties. Top left panel: mass accretion rate \dot{M} at the horizon for different spins. The blue points are the results of low resolution simulations, while the red points are the high resolution simulations. Top middle panel: the normalized MAD parameters for different spins. Plotted on top (green dashed line) the fit results of Narayan et al. (2022); Their formula is divided by $\sqrt{4\pi}/2$ to be consistent with our definition of MAD parameter, see Section 3.2 for more details. Top right panel: the jet efficiency as a function of spin. The green points are the predicted efficiencies and the blue (red) points are the efficiencies derived from our simulation (red- higher resolution). The error bars represent the 1 sigma temporal variation of each quantity. $\eta > 1$ represents more than 100% efficiency. Bottom left: the dependence of the slope $k \equiv (d\Phi_B/dt)/(d\dot{M}/dt)$ on the spin a . The slope k decreases as the spin a increases until $a = 0$, at which point the slope k begin to increase as a continues to increases. However, $a = 0.85$ slightly deviates from this trend. Bottom right panel: the time averaged disk height h/r given by Equation (15) as a function of radius.

on the black hole spin. First, as displayed by the dashed line, representing the time average of the mass accretion rate for $10^4 t_g < t < 2 \times 10^4 t_g$, prograde disks have a higher mass accretion rate than retrograde ones. The time-averaged accretion rate from $t = 10^4 t_g$ to $t = 2 \times 10^4 t_g$ is listed in Table 1 alongside the 1σ temporal variation. Second, the variation of the mass accretion rate is more pronounced in prograde disks than in retrograde disks.

The time evolution of the MAD parameter can be described as follows. As the accretion proceeds, the magnetic flux at the horizon accumulates until it saturates. At this point, the MAD parameter, as well as the magnetic flux threading the horizon and the mass accretion rate, are regulated by eruptions of magnetic flux. These eruptions expel the magnetic field to far distances from the black hole. In the MAD state, the pressure of the saturated magnetic field is balanced with the gas pressure (Bisnovatyi-Kogan & Ruzmaikin 1974; Narayan et al. 2003b). Although the flux eruptions cause the fluctuation in both the magnetic flux (Begelman et al. 2022) and the mass accretion rate, the MAD parameters generally remains stable around their time-averaged value.

To explore the differences in the MAD state for different spins, we present the time evolution of the MAD factors in Figure 3, where the left column is for negative spin simulations and the right column is for positive spin simulations, similar to Figure 2. The horizontal dashed lines represent the time-averaged MAD parameters from $t = 10^4 t_g$ to $t = 2 \times 10^4 t_g$, at which interval the MAD state is well established. The time-averaged MAD parameters during this period are also listed in Table 1. We find that the MAD parameters of prograde disks are higher compared to the corresponding retrograde disks. Additionally, similarly to the mass accretion rate, we find that the temporal fluctuations of the MAD parameters are greater for prograde disk. This is in agreement with the findings of Porth et al. (2021a), who also found that their co-rotating simulation has weaker flux expulsions than the counter-rotating case. We also observe many more small flux eruptions for the co-rotating case, but they are accompanied by several strong eruptions, such as the one at $\sim t = 9 \times 10^3$ for a94b100, as seen on Figure 3.

Both the mass accretion rate and the MAD parameter are strongly dependent on the black hole spin, a . This relation is displayed in the top left panel of Figure 4. We find that the mass accretion rate is highest for low, positive spin, and drops for higher values of the spin, both for prograde and retrograde disks, with retrograde disks show lower values than prograde disks. For the $a = 0$ spin we show two results, one with the standard resolution and one with a higher resolution, which we believe is more accurate (see discussion below). We also show in Figure 4 the 1σ temporal fluctuation of the mass accretion rate as error bars. Clearly, prograde disks have larger fluctuations (represented by larger error bars on Figure 4) than retrograde disks.

We present the relationship between the MAD parameters during the MAD state and the spin of black hole in the top middle panel of Figure 4. The MAD parameter increases as the spin increases from $a = -0.985$ to $a = 0.5$, and then decreases as the spin increases from $a = 0.5$ to $a = 0.985$. Narayan et al. (2022) reported a similar trend and used a third order polynomial to fit the relationship between a and the MAD parameter Φ_B . We include their fit result (displayed by the red dashed line) in the top middle panel of Figure 4 to compare with our results. Their definition of MAD parameters slightly differs from ours, so we renormalised their fit formula by a factor of $\sqrt{4\pi}/2$ to account for this discrepancy. Our results are in good agreement with theirs, which enhances credibility of the results considering that we use a different code, different resolutions, and shorter simulation duration.

Our simulations have a somewhat lower resolution (by a factor of ≈ 4) compared to Narayan et al. (2022); Chatterjee & Narayan (2022). To address this limitation, we conducted two simulations, aM94b100h and a0b100h, which have identical initial conditions as aM94b100 and a0b100, respectively, but differ by having a higher resolution. We show the mass accretion rates and the MAD parameters of these two simulations in Figures 2 and 3, alongside their counterpart with lower resolution. In the case of aM94b100 and aM94b100h, there is no significant difference in terms of mass accretion rates and MAD parameters. However, for a0b100 and a0b100h, the mass accretion rates are different by a factor of nearly three. According to White et al. (2019), this indicates a too low resolution for our simulation with spin $a = 0$ (but not for our simulations with rotating black-holes as is suggested by aM94b100h). They demonstrate that resolving the mass accretion rate demands a better resolution than to resolve the MAD parameter, as is also shown here. Indeed, the saturation values of the MAD parameters are nearly identical. This indicates that the properties of the MAD state should be similar.

Most of our simulations end at $t = 2 \times 10^4 t_g$. As discussed in sub-section 3.1, we extend aM94b100h to $t = 5 \times 10^4 t_g$. The time evolution of the mass accretion rate \dot{M} and of the MAD parameter Φ_B is shown in Figure 5. The MAD parameter remains relatively stable, oscillating around its average value, once the MAD state is established. However, the mass accretion rate \dot{M} gradually decreases until $t = 5 \times 10^4 t_g$, which is caused by the spread of the disk as the simulation advances.

3.3. Characteristic dynamical timescale

In the MAD state, magnetic flux eruptions play a major role in the dynamic of the accretion: the strong magnetic pressure pushes the gas out, which leads to the fluctuations of the accretion rate and of the magnetic flux. Moreover, these magnetic flux eruptions have been proposed as the origin of the Sgr A* flares observed in infrared by the GRAVITY collaboration (GRAVITY Collaboration et al. 2018, 2020). In particular, Dexter et al. (2020a) numerically estimated the recurrence time of the flare to be between 10^3 and $10^4 r_g/c$, corresponding to 5 to 50 hours for Sgr A*. The maximum of the intensity is correlated with the sharp drop of the MAD parameter at the onset of each eruption (Dexter et al. 2020a), lasting around a hundred r_g/c (Ripperda et al. 2022). The dynamic of a flux tube created in each eruptions was studied in details by Porth et al. (2021a). They found that the motion of the low-density/high magnetization region is at first strongly radial because of the magnetic tension, and then tends to circularize when the

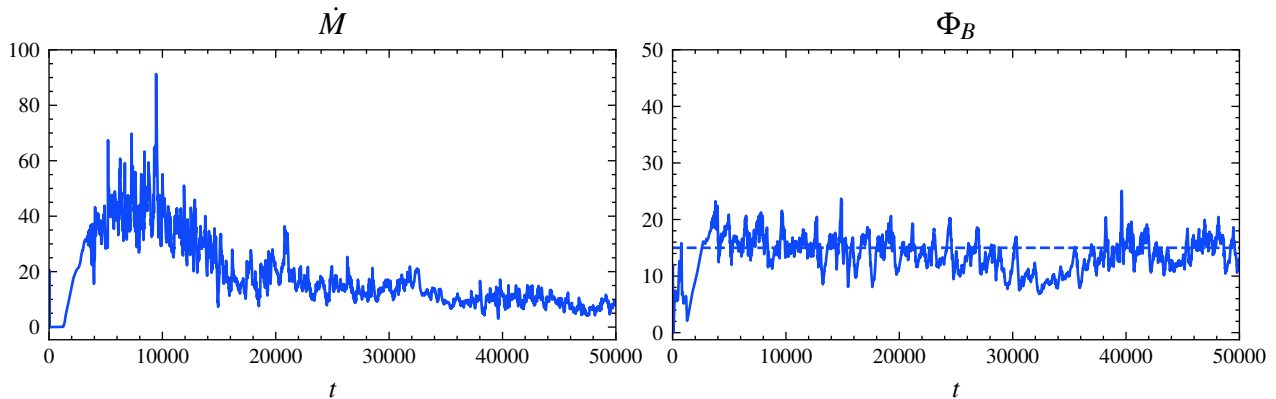


Figure 5. The long time evolution of the mass accretion rate and MAD parameters for simulation aM94b100h. The MAD parameter remains steady with time although the mass accretion drops.

field is nearly vertical. The typical life-time of these magnetic flux tubes was found numerically to be around 2 orbits, depending on their size and magnetic energy.

We use the discrete Fourier transform to study the duty cycle of the MAD parameters. The analysis is performed considering data from $t = 10^4 t_g$ to $t = 2 \times 10^4 t_g$ for which, as a preparation step, the time series are de-trended and their average removed, so that the fundamental Fourier coefficient is null. We show the power spectrum of the MAD parameter Φ_B for our simulations in Figure 6. We focus on the power spectrum from $f \simeq 4 \times 10^{-3}$ to $f \simeq 2 \times 10^{-4}$, which corresponds to the period from $T = 250 t_g$ to $T = 5000 t_g$. All our simulations show the same trend: after a few dominant peaks, the power spectrum decays proportionally to f^{-1} , characteristic of pink noise, which are shown as red dashed lines in Figure 6. Janiuk & James (2022) performed a similar study, not on the MAD parameter, but rather on the mass accretion rate. Furthermore, their disks are smaller than ours, with $r_{\text{in}} = 6$ or 12 and $r_{\text{max}} = 12$ or $25 r_g$. They found a power-spectrum of the mass accretion rate, which is well approximated with a power-law of index ~ 1.5 . They further report a dependence between the index and the black hole spin. Our analysis, on the other hand, does not show such a spin dependence on the index for the MAD parameter.

For some simulations, such as aM94b100 and a5b100, the power spectrum shows clear peaks in the frequency window preceding the onset of the noise. The corresponding periods are $t = 1,111 t_g$ for aM94b100 and $t = 1,666 t_g$ for a5b100. For the other simulations, no dominant time scale can be unambiguously identified. Previous identifications of a cyclic behavior of mass accretion rate and magnetic flux were published by, e.g., Chashkina et al. (2021). By analysing the data of their 2D GRMHD simulations, they found a period around $t \simeq 500 r_g/c$ (see also, e.g., Igumenshchev 2008; Dihingia et al. 2023). However, as noted by Chashkina et al. (2021), this pattern is an artefact due to the nature of 2D simulations, preventing non-asymmetric instabilities and phenomena, which are inherently responsible for the continuous accretion in 3D, to develop.

3.4. Relation between the MAD parameter and the mass accretion rate

The strong magnetic field during the MAD state pushes out the gas and stops, or at least regulates the dynamics of the in-falling of matter. Therefore, we naively expect that an increase of the magnetic flux should result in the decrease of the mass accretion rate, in other words, that they are anti-correlated. An anti-correlation is also expected if accretion proceeds by interchange instability, as matter replaces a highly magnetized region closer to the black hole resulting in a drop in the MAD parameter (Porth et al. 2021a). However, Porth et al. (2021a) did not find a correlation or an anti-correlation between \dot{M} and Φ_B . We expand their results for all black hole spins: none of our simulations show a correlation or an anti-correlation between \dot{M} and Φ_B .

We further studied the relation between the time-derivatives of the mass accretion rate \dot{M} and of the MAD parameter Φ_B . We first remove their average and de-trend the time series, then we use Fourier transformation to filter out the high (and weak) frequency components. We checked that this procedure does not change the results presented below. Instead, it allows for a better visualisation of the result. The processed time-derivatives are displayed in the left column of Figure 7 for aM94b100 and a94b100. The blue line is the normalized $d\dot{M}/dt$, and the red dashed line represents the normalized $d\Phi_B/dt$. Here, by "normalise" we mean that the two time-derivatives are stretched so that the maximum of their absolute value is 1. We show the resulting time series for aM94b100 and a94b100 as examples, but all other

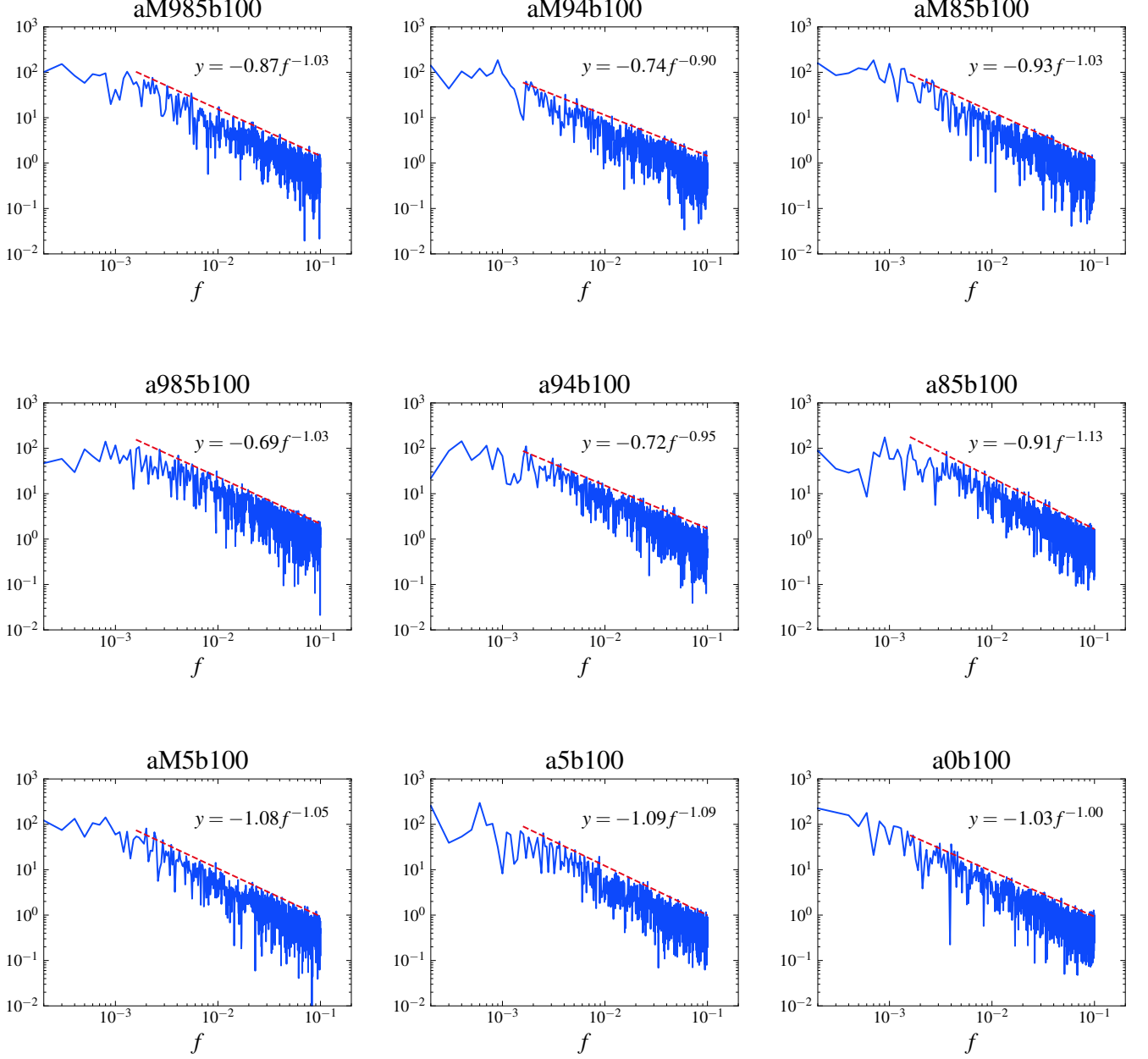


Figure 6. Power spectrum of the MAD parameters in the time interval $10^4 t_g < t < 2 \times 10^4 t_g$ ($1.5 \times 10^4 t_g$ to $2.5 \times 10^4 t_g$ for aM94b800). In all simulations, the power is concentrated in the low frequency region, which corresponds to periods about 500 – 2000 t_g . In the high frequency region, the power spectrum decreases following $\sim f^{-1}$. We use a red dashed line to show this evolution.

simulations exhibit a similar behavior. To the (positive) heights of $d\dot{M}/dt$ correspond the (negative) lows of $d\Phi_B/dt$ and vice-versa.

The time-derivatives of \dot{M} and Φ_B are clearly anti-correlated. In the right column of Figure 7, we show this anti-correlation. This means that when the mass accretion rate increases, the flux threading the horizon decreases. This can be understood as follows. Focusing in the region close to the equator, the horizon surface is separated into two regions: the accretion funnel from which the matter falls inward and the highly magnetized, low density regions of the magnetic flux eruption. As the MAD parameter increases, the magnetic pressure outside of the accretion funnel

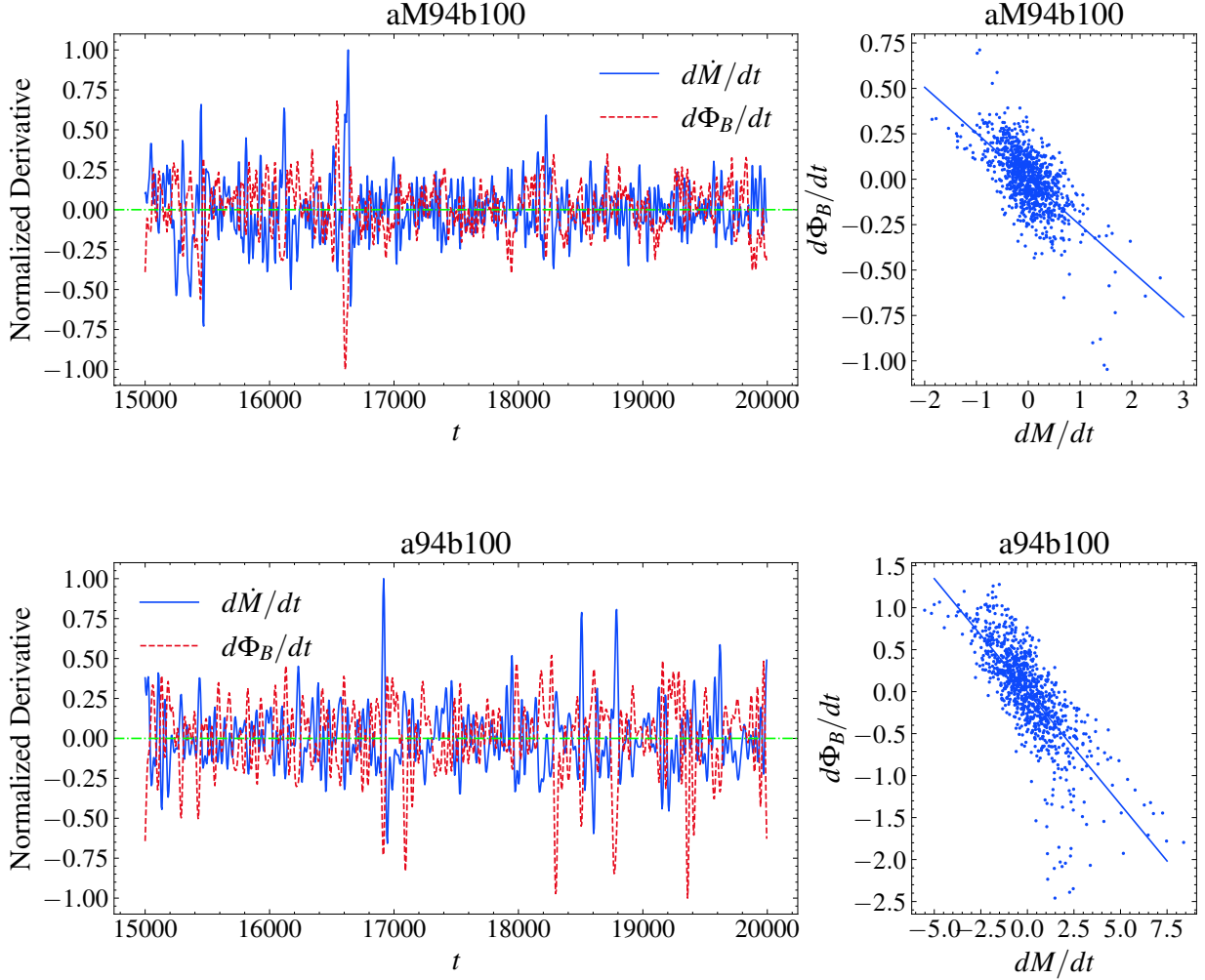


Figure 7. Left: time evolution of the time derivatives of the mass accretion rate and of the MAD parameter. We show the results for aM94b100 and a94b100, but other simulations also exhibit similar behaviors. These two quantities, $d\dot{M}/dt$ and $d\Phi_B/dt$ have opposite signs throughout the simulations. There is a clear anti-correlation between these two derivatives, shown in the right panels.

increases, and it gets compressed resulting in a lower accretion rate. Similarly, as the magnetic flux eruption develops, the magnetic flux at the horizon drops, thereby reducing the magnetic pressure and allowing for a larger accretion funnel and accretion rate. The latter is also enhanced by the interaction between the low density magnetic flux tube and the inner region of the turbulent disk at $r \sim 10 - 15 r_g$. Indeed, the magnetic flux tube velocity is sub-keplerian, reducing the velocity of the matter in the disk, which then falls "radially" onto the black hole.

We further perform a linear fit to this anti-correlation, and show the dependence of the slope $k \equiv (d\Phi_B/dt)/(d\dot{M}/dt)$ on the spin a in the bottom left panel of Figure 4. We find that the non-spinning black hole has the steepest slope k , which means that smaller variations in mass accretion rates correspond to larger variation in the MAD parameter, compared to other black hole spins. A smaller slope k is in general a characteristic of large absolute value of spin a , apart for $a = 0.5$ or for $a = 0.85$, which would deserve further investigations. Finally, we point out that the filtering performed in preparation to the data changes the value of k by a factor of up to about two, but the trend remains the same if one accounts for this re-scaling. We further note that there seem to be a strong dependence of k on the resolution, as is shown in the bottom left panel of Figure 4 by the two red dots, which are the slopes obtained from simulations aM94b100 and a0b100.

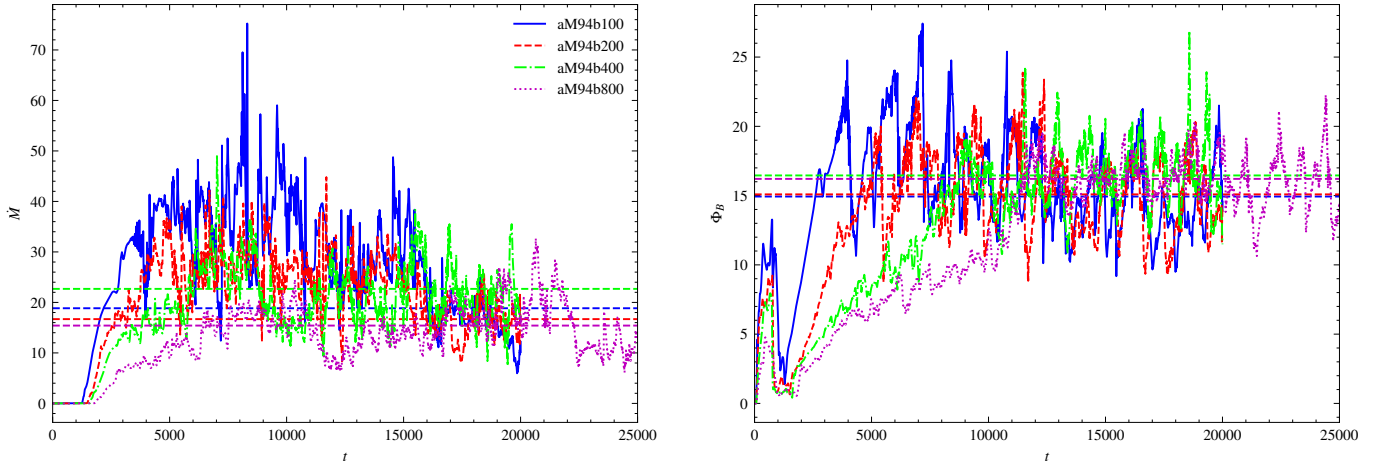


Figure 8. Mass accretion rates and MAD parameters of aM94b100, aM94b200, aM94b400, and aM94b800, which are simulations with the same initial conditions but with a different initial magnetic field strengths. In the left panel, we show the mass accretion rates. The larger the initial magnetization (the smaller β_0), the faster the mass accretion rate increases. After $t = 1.5 \times 10^4 t_g$, the mass accretion rates agree across all simulations. In the right panel, the MAD parameters of these simulations are shown to be consistent with each other after $t = 1.5 \times 10^4 t_g$. However, the time required to reach the MAD state is clearly different.

3.5. Jet efficiency

The jet efficiency, given by Equation (14) depends on the magnetic flux through the horizon normalised by the accretion rate \dot{M} . In agreement with many previous publications (see, e.g., Tchekhovskoy et al. 2011; Tchekhovskoy & McKinney 2012; McKinney et al. 2012; Narayan et al. 2022), we observe that the jet efficiency of positive spin black hole with $a > 0.5$ is on average larger than 100 %, meaning that the black hole is actually losing energy: the jet is powered by the Blandford and Znajek mechanism (Blandford & Znajek 1977).

We use the fitting formula proposed by Tchekhovskoy et al. (2010) and latter used by Narayan et al. (2022) to interpret the efficiency, namely

$$\eta = \frac{\kappa}{4\pi} \Omega_H^2 \Phi_B^2 (1 + 1.38\Omega_H^2 - 9.2\Omega_H^4). \quad (19)$$

Here $\kappa = 0.08\sqrt{\pi}$ is a numerical constant and $\Omega_H = ac/r_H$ is the angular velocity at the horizon. This value of κ is chosen such that $\sqrt{\pi}$ accounts for the difference in the definition of Φ_B used here and in Tchekhovskoy et al. (2010), and the numerical factor 0.08 is chosen to match the normalisation of our numerical data. The predicted efficiency, *i.e.* using the measured value of the MAD parameter Φ_B together with Equation (19), and the simulated efficiency, namely directly measured from our simulations as defined by Equation (14) are shown in the right panel of Figure 4 as a function spin. It is clear that they are consistent with each other. Narayan et al. (2022) reported the same behavior but used a different value of $\kappa = 0.05$ differing from our normalisation by a factor smaller than 2. This discrepancy could be due to the time at which the measurements are performed. Indeed, when averaging the results of simulation aM94b100h at late times, $10^4 t_g < t < 5 \times 10^4 t_g$, we find a lower numerical factor of ~ 0.06 .

3.6. Effects of the initial magnetic field strength

Since the magnetic field plays a critical role in the accretion process and its regulation, we wish to assess the solidity of our result with respect to the initial magnetic field strength. To this end, we also performed simulations with different values of β_0 for $a = -0.94$. In Table 1, we list three additional simulations with initial magnetic field strength $\beta_0 \in 100, 200, 400, 800$. The simulation aM94b100 has the strongest initial magnetic field strength, while aM94b800 has the weakest.

In Figure 8, we present the mass accretion rates and MAD parameters for those additional simulations with different initial magnetic field β_0 . The left panel shows that at the beginning of the accretion process, the mass accretion rate \dot{M} increases with the initial magnetic field strength, which can be attributed to the fact that the transfer of angular momentum is initially driven by MRI, which development depends on the strength of the magnetic field. Therefore, the larger the initial magnetic field, the higher the mass accretion rate. However, at late time $t > 15,000 t_g$, we see that the mass accretion rates achieve similar values across all simulations.

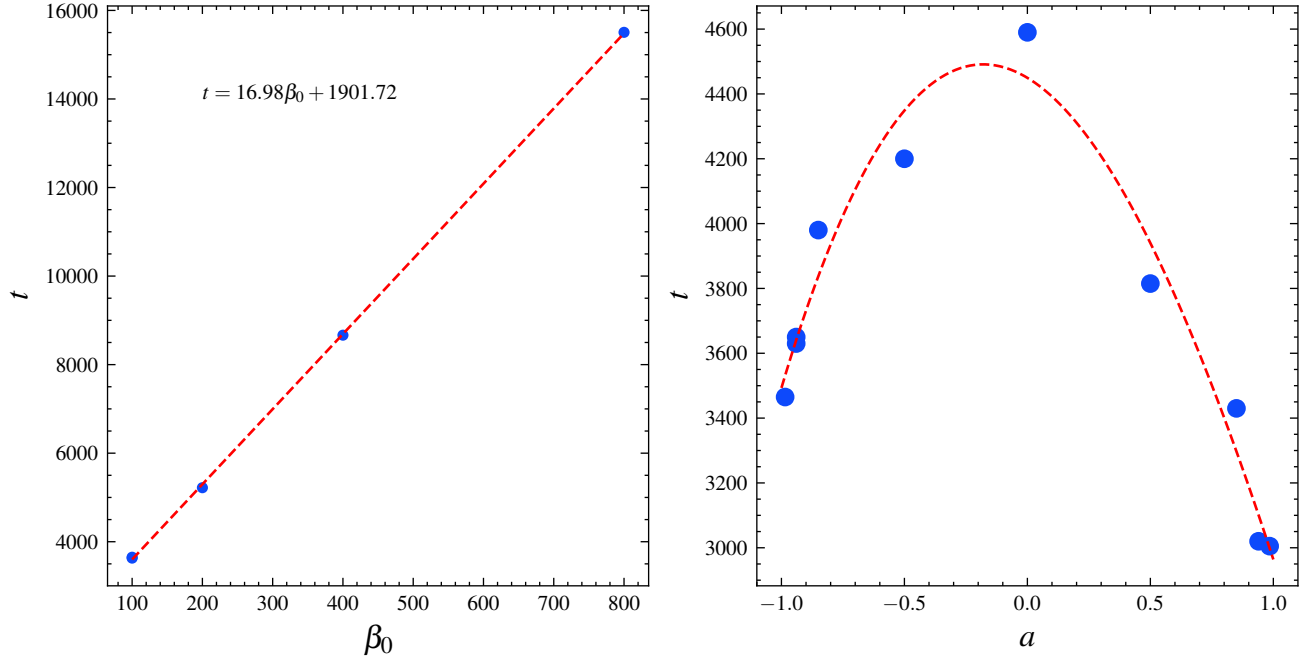


Figure 9. Left Panel: The relation between the coasting time t_{MAD} to reach the MAD state and the initial magnetic field. We show the results for aM94b100, aM94b200, aM94b100h, aM94b400, and aM94b800 in blue circles. The coasting time linearly depends on the initial magnetic field. We use a linear function to fit it, and the best fit result is shown by the red dashed line. Right Panel: The t_{MAD} as a function of the value of the spin a . We use a third order polynomial function to fit this relation, and the best fitted result is shown by the dashed red line.

In the right panel of Figure 8, it is seen that the MAD parameters also achieve similar values across all simulations during the MAD state, here reached after $t > 15,000t_g$ specifically for aM94b800. This suggests that the MAD state is independent of the initial magnetic field strength. However, the time required to reach the MAD state varies. To investigate the dependence of the required time on the initial β_0 , we use the following criteria to define t_{MAD} , which is the time required to reach the MAD state

1. The mean MAD parameter averaged from $t = t_{\text{MAD}}$ to $t = t_{\text{MAD}} + 1000 t_g$ should be larger than the 1σ lower limit of the final MAD parameter.
2. The MAD parameter in the MAD state should be highly variable. Therefore, we require the derivative of the MAD parameter to change sign several times between $t = t_{\text{MAD}}$ to $t = t_{\text{MAD}} + 1000 t_g$.

According to these two criteria, the time it takes to reach the MAD state t_{MAD} for aM94b100, aM94b100h, aM94b200, aM94b400 and aM94b800 is $3650 t_g$, $3630 t_g$, $5220 t_g$, $8665 t_g$ and $15505 t_g$, respectively. In the left panel of Figure 9, we display the time required to reach the MAD state as a function of the initial magnetic field strength β_0 . We find that t_{MAD} increases linearly with β_0 , namely it increases as the initial magnetic field strength weakens. The best fitting result is a linear function, $t_{\text{MAD}} = 17\beta_0 + 1.9 \times 10^3$. This result suggests that the accumulation of the magnetic flux linearly depends on the initial magnetic field strength. We also study the dependence of t_{MAD} on the spin for the other simulations with the same initial β_0 . The right panel of Figure 9 displays the dependence of t_{MAD} on the spin a . As the spin increases from $a = -1$ to $a = 0$, t_{MAD} increases. It then decreases as a increases from 0 to 1. This dependence is fitted with a third order polynomial which results in $t_{\text{MAD}} = 1.9 \times 10^2 a^3 - 1.2 \times 10^3 a^2 - 4.6 \times 10^2 a + 4.4 \times 10^3$.

3.7. Evolved disk and jet structures

The strong magnetic field at the center of the accretion system shapes the disk and launches the bipolar jet at low radii. Therefore, the disk structure is an important characteristics of the MAD state. In the bottom right panel of Figure 4, we show the time-averaged disk height h/r , which is averaged from $t = 10^4 t_g$ to $t = 2 \times 10^4 t_g$. We find that retrograde disks are thicker than prograde disks. In the inner region ($5r_g < r < 15r_g$), the disk height increases as the

absolute value of the spin increases, which is consistent with the results of [Narayan et al. \(2022\)](#). However, contrary to the findings in this aforementioned paper, we find that the non-spinning black hole has the thinnest disks of all, while they argued that the disk of the non-spinning black hole is thicker than that of prograde disks. A possible explanation to this discrepancy is the fact that our analysis is carried at earlier times.

We show the time and azimuthal averages of the density ρ , of the plasma parameter β and of the magnetization σ for the simulations aM94b100, a94b100 and a0b100 in Figure 10. These values are obtained using Equation 16, and are then averaged from $t = 10^4 t_g$ to $t = 2 \times 10^4 t_g$. The difference between these three spins is clear. In the density ρ plot, the non-spinning black hole has the thinnest disk, while the prograde disk is the thickest, which is consistent with the bottom right panel of Figure 4. The β plots show similar behaviors as the density. There are clear vacuum regions inside the jet, especially for a0b100, which are attributed to the numerical flooring rather than physical effects.

We show the polar angle of the jet boundary, which we associate to $\sigma = 1$, as a function of radius for aM94b100, a94b100 and a0b100 in the left panel of Figure 11. The vertical lines correspond to 1σ variations and the points represent the median values of the polar angle θ for a specific radius r . These values are obtained for $10^4 t_g < t < 2 \times 10^4 t_g$. As shown in Figure 3, all three runs remain in the MAD state during this time period, and maintain inflow-outflow equilibrium. It is seen that the prograde disk has a wider jet than the retrograde at $r < 20r_g$, which is consistent with the findings of [Narayan et al. \(2022\)](#). It is also clearly seen that the non-spinning black hole has the widest jet. This result is consistent with Figure 10.

In order to quantify the degree of variation compared to their mean, we use the standard error $\sigma_\theta/\bar{\theta}$, where σ_θ is the 1σ variations of θ and $\bar{\theta}$ is the median. The temporal and radial (between $2r_g$ and $30r_g$) averages of $\sigma_\theta/\bar{\theta}$ for aM94b100, a94b100 and a0b100 are 0.11, 0.08 and 0.07, respectively. We further show the kernel density estimation of $\theta_{\sigma=1}$ at $r = 10r_g$ in the right panel of Figure 11. The boundary of the retrograde disk has the largest variations, as expected from large shear stresses at the boundary between the jet and the disk, which have opposite toroidal velocity. Our results are, in this sense, consistent with those of [Wong et al. \(2021\)](#), who argued both analytically and numerically that retrograde disks have stronger shear across the jet-disk boundary than prograde ones.

3.8. Pressure

In section 3.7, we demonstrated that prograde disks are thinner and have wider jets. We attribute these to the pressure distribution inside the disk and jets. In Figure 12, we show the different components of the magnetic pressure and of the gas pressure for aM94b100, a0b100 and a94b100. These components are calculated using Equation (18) and are further time-averaged. This implies that they are biased towards large density regions. We find that the overall total pressure $p + b^2/2$ is the lowest for non-rotating black hole and the largest for prograde disk. At small radii, the magnetic pressure b^2 , represented by the blue line, dominates over the gas pressure. As the radius increases, the gas pressure gradually becomes dominant. The transition radius for $a = 0.94, 0, -0.94$ are $r_{eq} = 2.71r_g, 3.13r_g, 2.35r_g$, respectively.

[Begelman et al. \(2022\)](#) analyzed a prograde disk, which is somewhat smaller than the ones we analyze here. They reported that the gas pressure evolves $\propto r^{-2}$ while the magnetic pressure was found to evolve faster closest to the black hole. Here we find that the gas pressure evolution is somewhat steeper than r^{-2} . This could be due to the different disk structure, different resolution we are using or the shorter time interval over which the averaged is performed. We note that a similar radial evolution of the gas pressure, namely $p_g \propto r^{-2}$ was reported by [Tchekhovskoy et al. \(2011\)](#) and [McKinney et al. \(2012\)](#) who found that $p_g \propto r^{-1.9}$ for their "thinner" disk models.

We further show in Figure 12 the radial dependence of all individual magnetic pressure components. The total magnetic pressure has a similar radial evolution in our work and in the work of [Begelman et al. \(2022\)](#), namely its radial evolution is steeper than r^{-2} close to the black hole. As is seen from Figure 12, the polar component b_θ^2 never dominates for any of the spins and is much lower than the radial and toroidal components. Second, at small radii inside the ISCO, the main difference between rotating and non-rotating black holes is the contribution of the toroidal field b_ϕ^2 : it is negligible compared to the radial component for a non-rotating black hole, while both components are of the same order for rapidly rotating black holes. The toroidal field even dominates for the prograde disk very close to the black hole. This explains the difference between the conclusions of [Begelman et al. \(2022\)](#), who studied disks around rapidly rotating black holes, and [Chatterjee & Narayan \(2022\)](#) who studied non-spinning black hole systems, which is the importance of the toroidal component in a MAD accretion process. Similar radial evolution of the magnetic field components were reported by [Tchekhovskoy et al. \(2011\)](#) and [McKinney et al. \(2012\)](#) who found that $b_r \propto r^{-1.5}$ and

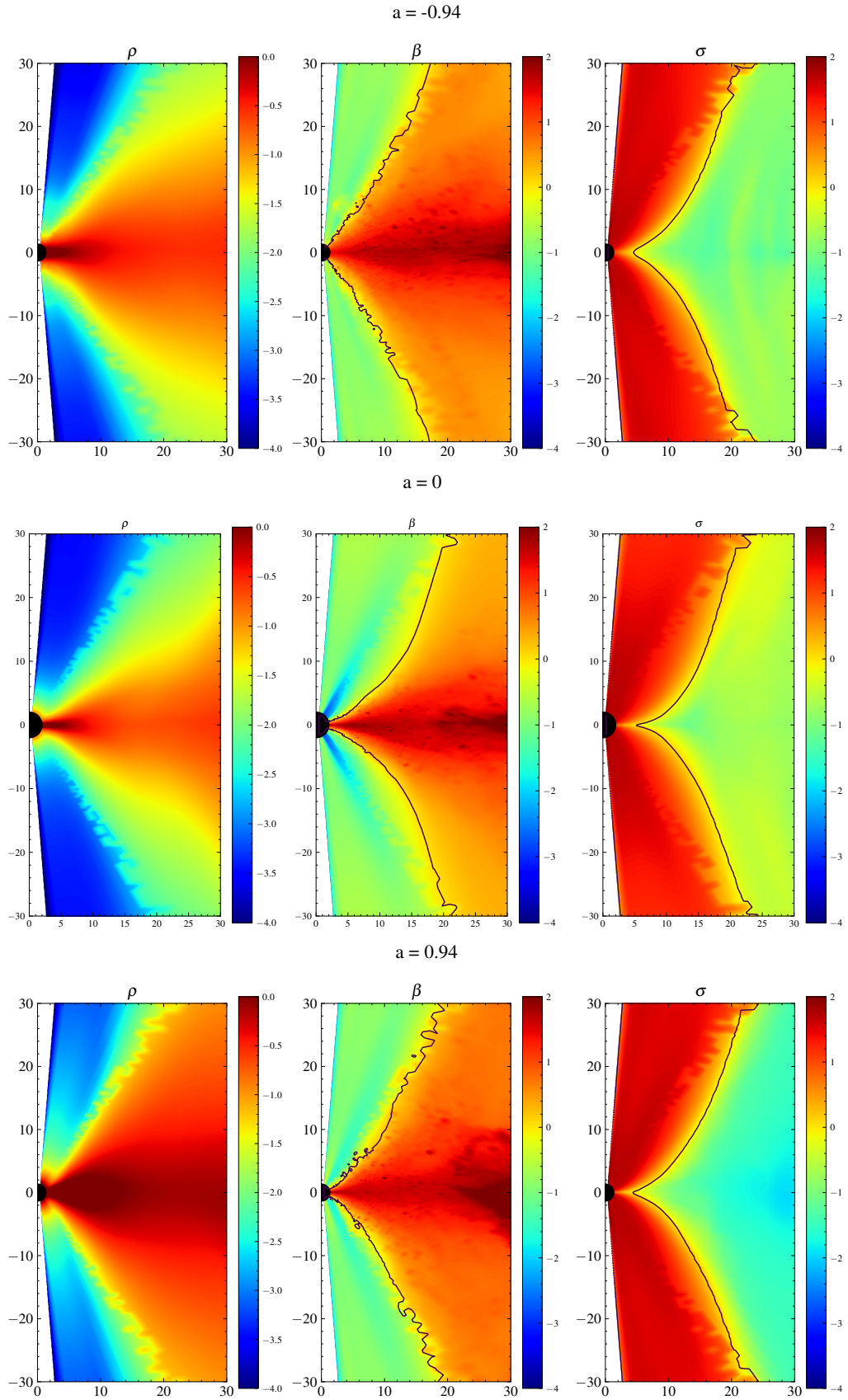


Figure 10. Time and azimuthal averaged density ρ , ratio of gas to magnetic pressure β and magnetization σ for aM94b100 (top), a0b100 (middle) and a94b100 (bottom). The black lines in the middle and right panels represent the $\beta = 1$ and $\sigma = 1$ conditions, respectively.

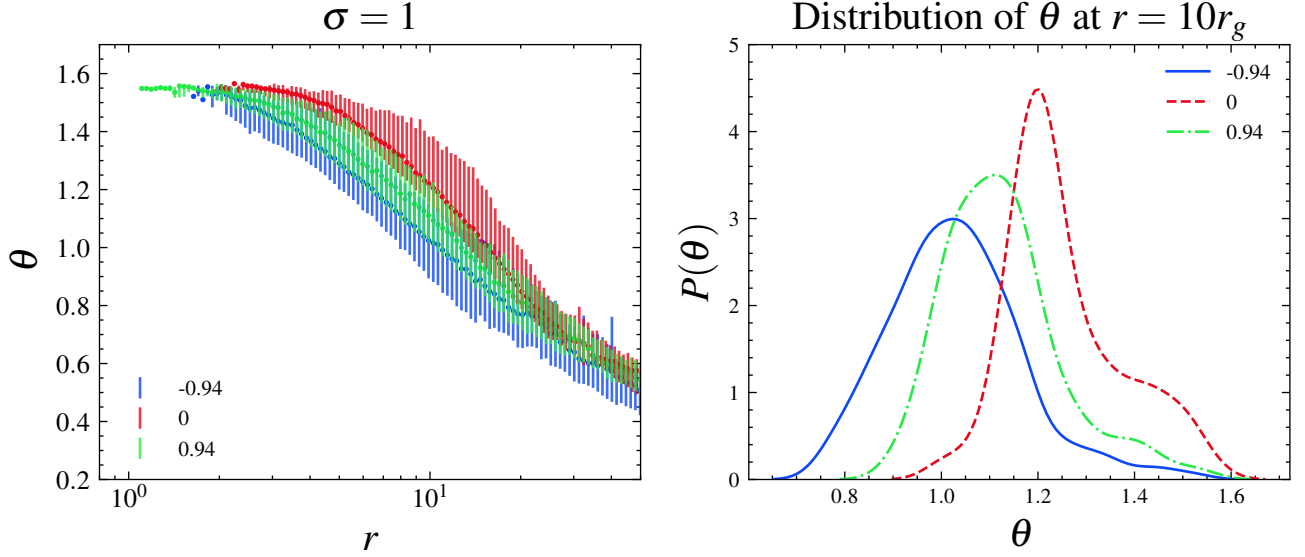


Figure 11. Left Panel: The 1σ region of jet boundary for $a = -0.94, 0$ and 0.94 . We use the magnetization parameter $\sigma = 1$ condition as the jet-disk boundary and derive the 1σ variations and median of the polar angle θ for $\sigma = 1$ at a given radius r . The vertical lines are 1σ variations and the dots are the median values. Right Panel: The kernel density estimation (KDE) of the polar angle θ such that $\sigma = 1$ at radius $r = 10r_g$. The non-spinning black hole has the widest jet, corresponding to the largest θ , while the prograde disk with $a = 0.94$ has a wider jet than the retrograde disk with $a = -0.94$. In addition, the non-spinning black hole has the narrowest peak, which suggests that the jet boundary of a non-spinning black hole is the most stable.

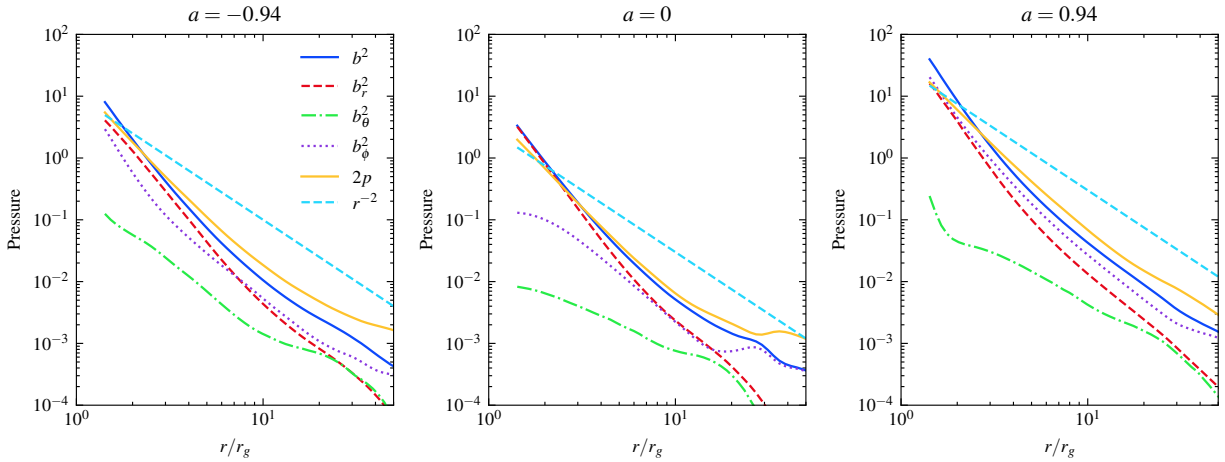


Figure 12. The angular- and time-averaged gas pressure p (yellow) and magnetic pressure b^2 (blue) for aM94b100, a0b100 and a94b100. We further show each component of the magnetic pressure, b_r^2 (red), b_θ^2 (green) and b_ϕ^2 (purple). These values are calculated by Equation 18 and then time-averaged. The dashed (light blue) curve represents an r^{-2} dependence.

$b_\phi \propto r^{-1}$ for their "thinner" disk models. Clearly, the radial dependence of b^r does not seem to depend on the black hole spin, while the toroidal component does.

We show the ϕ - and time- averaged maps of the pressure components of- aM94b100, a0b100 and a94b100 in Figure 13. All sub-figures use the same color scaling, allowing an easy comparison between them. At small radii close to the black hole, the radial component b_r^2 are large for all three simulations and decrease quickly as the radius increases. For $a = \pm 0.94$, large values of b_r^2 are also found at large radii $r \sim 10r_g$ in the jet region. The polar component, b_θ^2 , is negligible in all three cases. Note that the blank regions in the color-maps of b_θ^2 are caused by numerical truncating errors: this component is too small relative to the other two components. The distributions of the toroidal component b_ϕ^2 also shows a great variance. The non-spinning black hole has the weakest b_ϕ^2 component, while it is larger for the

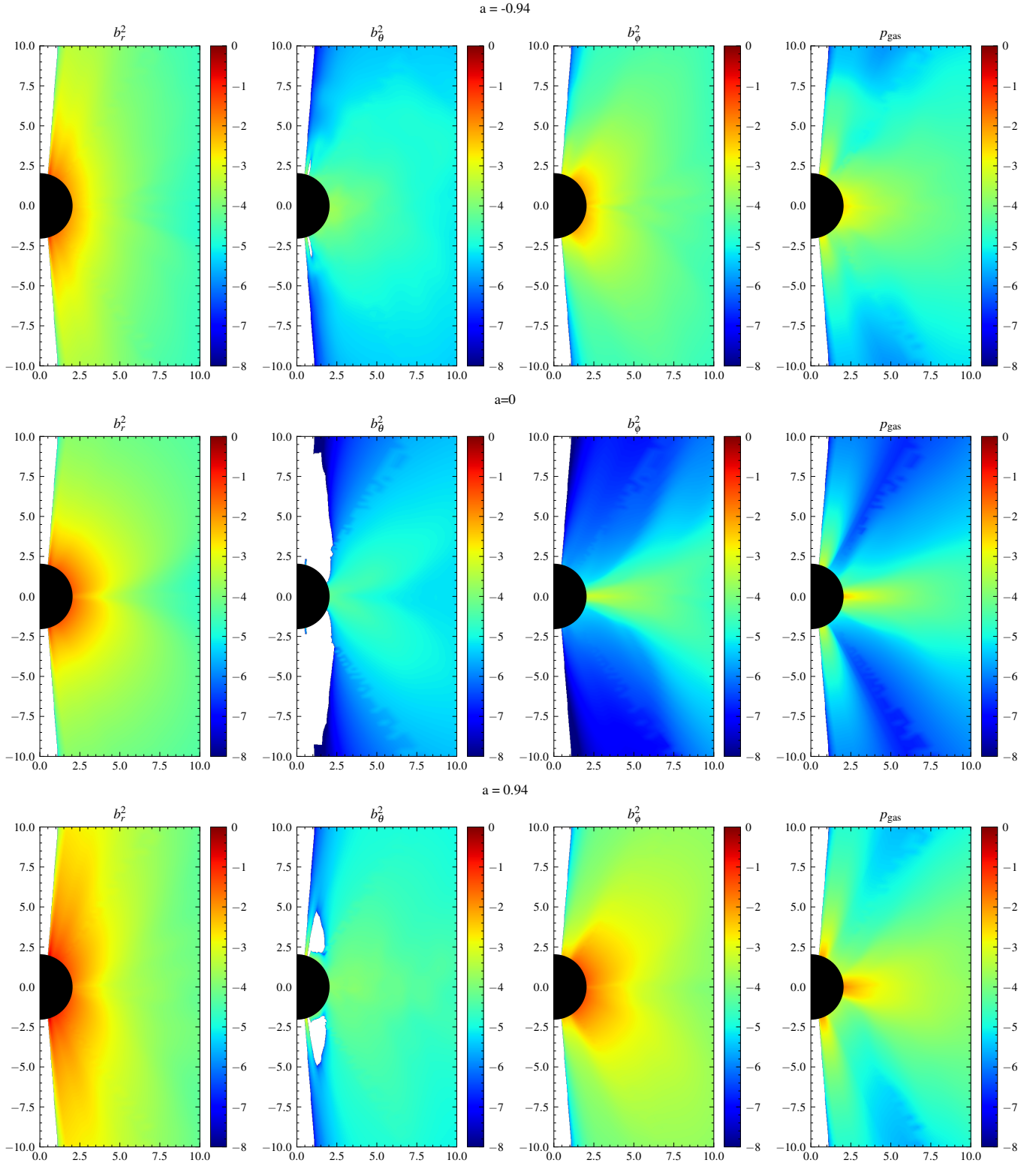


Figure 13. The time and azimuthal averages of the magnetic pressure components, namely b_r^2 (first column), b_θ^2 (second column), and b_ϕ^2 (third column), and of the gas pressure (last column) for $a = -0.94$ (top), $a = 0$ (middle) and $a = 0.94$ (bottom). The color scaling is the same for all spins and all components to better display the differences. The most striking difference is the small contribution of the azimuthal component b^ϕ to the total magnetic pressure for the non-spinning black hole $a = 0$.

spinning black holes. We note the drop of $|b^\phi|^2$ at the equator: this is because b^ϕ changes sign at the equator due to the presence of a current sheet separating the two hemispheres. This drop is more pronounced and visible for the spinning black holes.

The gas pressure p_g of the non-spinning black hole contains clear weak channels about $\theta \simeq \frac{\pi}{3}$ and $\theta \simeq \frac{2\pi}{3}$. These channels are also visible for the spinning black holes, but are less pronounced. As we previously discussed in section 3.7, these channels are caused by the numerical floors applied in the regions closest to the pole, which are required to maintain numerical stability in our simulations.

4. ANGULAR MOMENTUM FLUX

It has long been argued that magnetic fields drive the transfer of angular momentum during accretion via the development of the magneto-rotational instability (Balbus & Hawley 1991b, 1998b), but also by helping to launch a disk wind and producing a strong jet, both components capable of significantly transporting angular momentum. In this section, we investigate the dependence of angular momentum flux on the spin of the black hole. We use the definitions in Chatterjee & Narayan (2022) to define the total angular momentum flux \dot{J}_{total} , the advected angular momentum flux \dot{J}_{adv} and the angular momentum flux due to stresses \dot{J}_{stress} ,

$$\dot{J}_{\text{total}}^i(r, \theta) = \langle T_{\phi,t}^i \rangle_{\phi,t} \quad (20)$$

$$\dot{J}_{\text{adv}}^i(r, \theta) = \left\langle \left(\rho + u_g + \frac{b^2}{2} \right) u^i \right\rangle_{\phi,t} \langle u_\phi \rangle_{\phi,t} \quad (21)$$

$$\dot{J}_{\text{stress}}^i(r, \theta) = \dot{J}_{\text{total}}^i(r, \theta) - \dot{J}_{\text{adv}}^i(r, \theta) \quad (22)$$

where $\langle X \rangle_j$ represent the average of X with respect to variable j . Note that for this section, there is no weighting by the density ρ . We further decompose the stressed induced angular momentum flux into its Maxwell $\dot{J}_{\text{stress,M}}$ and its Reynolds $\dot{J}_{\text{stress,R}}$ components:

$$\dot{J}_{\text{stress,M}}^i(r, \theta) = \left\langle \frac{b^2}{2} u^i u_\phi - b^i b_\phi \right\rangle_{\phi,t} \quad (23)$$

$$\dot{J}_{\text{stress,R}}^i(r, \theta) = \left\langle \left(\rho + u_g + \frac{b^2}{2} \right) u^i u_\phi \right\rangle_{\phi,t} - \dot{J}_{\text{adv}}^i \quad (24)$$

Following these definitions, the time- and ϕ -averaged angular momentum flux in the radial direction of a94b100, a0b100 and aM94b100 are shown in Figure 14 at three different radii, namely $10r_g$, $15r_g$ and $20r_g$.

For non-spinning black hole, depicted in the middle line of Figure 14, the results we obtained are similar to the results reported in Chatterjee & Narayan (2022). The radial component of the total angular momentum flux \dot{J}_{total}^r is negative in the disk region at all sampled radii, $r = 10r_g$, $15r_g$, and $20r_g$. This indicates that as the matter accretes, it brings a net angular momentum to the black hole. However, at $\theta \simeq 0.35\pi$ and 0.65π , the total angular momentum flux changes sign to become positive. This shows that angular momentum is being transported away from the accretion disk by the wind. The radial angular momentum flux converges to 0 as it approaches the poles, underlying the weakness of the jet for $a = 0$. In the disk, the contributions of \dot{J}_{adv}^r and $\dot{J}_{\text{stress,R}}^r$ dominate and are always negative, suggesting that they are responsible for the inward transport of angular momentum in the disk, as was previously demonstrated by Chatterjee & Narayan (2022). We note that the relative importance of the Reynolds components is large at small radii but decreases towards large radii and is in agreement with the results of Chatterjee & Narayan (2022) at $r = 20r_g$. Furthermore, the Maxwell stress component $\dot{J}_{\text{stress,M}}^r$ is always positive with two maxima, reached at $\theta \simeq 0.4\pi$ and $\theta \sim 0.6\pi$. At these high latitudes, the radial component of the total angular momentum flux is dominated by $\dot{J}_{\text{stress,M}}^r$ underlying the importance of magnetic fields in the production and dynamics of the wind above the disk in the transport of angular momentum.

The results of the black hole with positive spin $a = 0.94$ are displayed in the top line of Figure 14. We find this case to be qualitatively similar to the non-spinning black hole scenario: the radial component of the total angular momentum flux is negative in the disk and positive at high latitudes, with a change of sign at $\theta \sim 0.4\pi$ and $\theta \sim 0.6\pi$. Outside the disk, we find that the Maxwell component strongly dominates and reaches its maxima symmetrically with respect to the equator at $\theta \sim 0.25\pi$ and $\theta \sim 0.75\pi$. The radial components of the angular momentum flux remain large up to the poles. This indicates the existence of powerful magnetized winds and jets, through which the disk and

the black hole lose a substantial fraction of their angular momentum. We further see that the angular momentum flux contributed by advection is negative in the disk region. However, it is positive at high latitude, which is different from the case of the non-spinning black hole. This may be due to the large contribution of the magnetic fields energy density $b^2/2$ in its expression. Finally, we find that the Reynolds stress component is much smaller than any of the other components and can be safely ignored.

For the negative spin simulation $a = -0.94$ displayed in the bottom line of Figure 14, we find that the radial angular momentum flux distribution with angle is significantly distinct from that of the non-rotating and positive spin black holes. This is mostly due to the fact that the poloidal velocity changes sign: the plasma corotate with the black hole close to the pole while it corotates with the disk at the equator. First, we find that the radial component of the total angular momentum flux is always negative at all angles. As a result, the black hole gains angular momentum and its spin decreases towards 0. This is consistent with the result presented in Figure 1. The contribution of the advection to the flux of angular momentum is similar to the cases of positive and null spins, namely its contribution is maximum and negative at the equator. The Maxwell component contribution is positive at the equator, showing that magnetic fields are responsible for taking away radial angular momentum also in this case. However this contribution is negative around $\theta \simeq 0.2\pi$ and 0.8π and dominates the radial total angular momentum flux at those angles.

The signs of angular momentum flux are mainly determined by the sign of the azimuthal velocity u_ϕ and of $b^r b_\phi$. In Figure 15, we show the ϕ - and time-averaged evolution of u_ϕ and of $b^r b_\phi$ with the polar angle θ at the three radii selected for the angular momentum flux in Figure 14. For the $a = 0$ and $a = 0.94$ cases, the toroidal velocity u_ϕ is positive for all angles θ as expected, therefore, the sign of the advection contribution to the angular momentum flux \dot{J}_{adv} depends on the sign of u^r . On average, u^r is negative in the disk region since the matter is accreted towards the black hole. It is however positive at high latitude, as matter is carried away in the disk wind and the jet. This change of sign explains the pattern of \dot{J}_{adv} seen in Figure 14 for $a = 0.94$. For the non-spinning black hole, the azimuthal velocity quickly goes to 0 at high latitude, which explains the null contribution of the advection to the angular momentum flux in this region. On the other hand, the term $b^r b_\phi$ is always negative at all angles θ for the black hole with spin $a = 0.94$. In this case, the maxima (one in each hemisphere) of $|b^r b_\phi|$ is reached closer to the poles than for the non-rotating black hole, further underlying the different disk structure: rotating black holes have wider disk than non-rotating ones, as was already demonstrated in Section 3.7 and in Figures 10 and 11. The polar angles θ at which the maxima of $b^r b_\phi$ are reached correspond to the angle at which the contribution of the Maxwell stress is maximal.

The actual sign of the component $b^r b_\phi$ depends on our arbitrary choice of initial disk magnetization, and specifically on the orientation of the initial magnetic field loop. A different orientation would lead to a different sign of the $b^r b_\phi$ component. Indeed, the sign of b_ϕ is set by frame-dragging and it is positive in the south hemisphere and negative in the north hemisphere, for prograde disks. However, the sign of b^r would be opposite if the initial magnetic field loop would have had a different orientation, as demonstrated in McKinney et al. (2012). We note here another difference between the $a = 0$ and $a = 0.94$ black holes: $b^r b_\phi$ is negative close to the poles for the rotating black hole, while it is very small for the non-rotating black hole.

The situation is different for the retrograde disk, with a different evolution of the azimuthal velocity u_ϕ and of the term $b^r b_\phi$ with polar angle θ , both shown in the third line of Figure 15 for $a = -0.94$. The toroidal velocity u_ϕ is also positive in the disk region. However, it becomes negative close to the poles around $\theta \simeq 0.2\pi$ and $\theta \simeq 0.8\pi$. The term $b^r b_\phi$ is also different from that of the prograde disk. First, it has a different sign close to the pole: $b^r b_\phi$ is positive for a retrograde disk since (i) b_ϕ is negative in the south hemisphere and positive in the north hemisphere because of frame dragging, and (ii) b^r is negative in the south hemisphere and positive in the north hemisphere. Here, the sign of b^r is set by the orientation of the initial magnetic field loop. At the equator, however, $b^r b_\phi$ has the same sign for both prograde and retrograde disks. This explains the sign of the Maxwell stress contribution to the radial angular momentum flux.

In order to understand how angular momentum is transported throughout the disk, we show in Figure 16 colormaps of the angular momentum flux modulus

$$\dot{J}^2 = (\dot{J}^r)^2 + (\dot{J}^\theta)^2, \quad (25)$$

for the total, advection and Maxwell stress components and the associated streamlines. The top line shows the total angular momentum flux, while the middle and bottom lines show the contribution of the advection and Maxwell stress, respectively. The left, middle and right columns are for spins $a = -0.94, 0, 0.94$ respectively. We note that the scale of the color coding is the same in each line to ease the comparison between the different black hole spins. Further, we point out that the equilibrium radius for these simulations is around $r = 30r_g$, prompting caution for larger radius.

First, it is clear that each of these figures is antisymmetric with respect to the equator, as expected. We note that these figures are obtained directly from the data from our simulation without imposing the symmetry as done by Chatterjee & Narayan (2022). From the top line, we further see that for all three spins, angular momentum is lost by the disk through the disk wind.

There is one more difference between those figures: the angular momentum flux at the pole is negative for $a = -0.94$ and $a = 0$, while it is positive for $a = 0.94$. Also, the contribution to the total angular momentum flux in this region appears to be small compared to the flux at the equator as seen in Figure 14. In addition, Figure 16 shows the presence of a transition layer in the simulation with a negative and a null spin. In this transition layer, the angular momentum flux changes direction, being oriented outwards in the wind and inward in the jet. The position of this transition layer is at larger angle from the pole for $a = -0.94$ than for $a = 0$. This transition layer also appears in the Maxwell stress contribution.

The streamlines of the Maxwell stress contribution to the total momentum flux are shown in the last line of Figure 16. We find two interesting features. First both the prograde and retrograde disks display a large Maxwell stress contribution to the angular momentum flux in the jet region contrary to the non-spinning black hole. This underlines that the jets of a non-rotating black hole in the MAD regime are weak and do not transport a substantial amount of angular momentum (and in fact energy) to their surrounding environments. The largest outward contribution in the non-rotating black hole actually comes from the magnetized wind. It is also clear that the jet of the prograde disk is stronger than that of the retrograde black hole and deposit angular momentum faster into its environment. We further see a substantial Maxwell stress contribution into the wind, which shares the same characteristics as the total angular momentum flux, meaning it is weaker for retrograde disks. Finally, we find that for the retrograde disk, a region of nearly zero Maxwell stress contribution separates the wind region from the disk region. This transition is associated with the change of sign of the toroidal velocity u^ϕ , shown by the red line in Figure 16 for $a = -0.94$. It is clear that the red line follows the transition region.

5. CONCLUSION

In this work, we performed several GRMHD simulations of thick accretion disks in the MAD regime around black holes characterized by different spin a with cuHARM. Our key results can be summarized as follows:

1. We studied the angular momentum flux for our simulations with $a = -0.94, 0, 0.94$ and underlined the differences. We found that i) a substantial amount of angular momentum is transported away in the magnetized wind and that the Maxwell stresses are larger for rotating black hole than for non-rotating black hole as expected because of frame-dragging. In fact, the amount of angular momentum transported by the "jet" for the non-rotating black hole is small and negligible. These results were provided in Section 4 and are clearly displayed in Figure 16.
2. We did not find any correlation between the mass accretion rate and the MAD parameter. However, we did find an anti-correlation between their time derivatives, displayed for our simulations aM94b100 and a94b100 on Figure 7. We provided a heuristic explanation for this result in Section 3.4.
3. We underlined the difference in the magnetic field component strengths for spinning and non-spinning black holes in Section 3.8. From Figures 12 and 13, it is seen that the θ component is always subdominant, while the relative importance of the ϕ component depend on the spin of the black hole. In the non-rotating case, the toroidal component is negligible compared to the radial component close to the horizon, while these components are comparable for the rotating black hole. The toroidal component even dominates very close to the horizon for $a = 0.94$. We therefore recover both results from Begelman et al. (2022) and Chatterjee & Narayan (2022) on the importance of the toroidal component in regulating the accretion, and confirmed that the difference has its origin in the black hole spin.
4. We underlined the differences in the structure of the disks and the jets in the MAD state as a function of spin in Section 3.7. In particular, we found that retrograde disks are wider than the corresponding prograde disks, in agreement with the findings of Narayan et al. (2022). Correspondingly, the jets of prograde disk are narrower than the jets of retrograde disks. These results are displayed in Figure 11.
5. We studied the MAD parameters and investigated their dependence on the spin and the initial magnetic field strength in Sections 3.2 and 3.6. We found that our numerical results are in very good agreement with those of

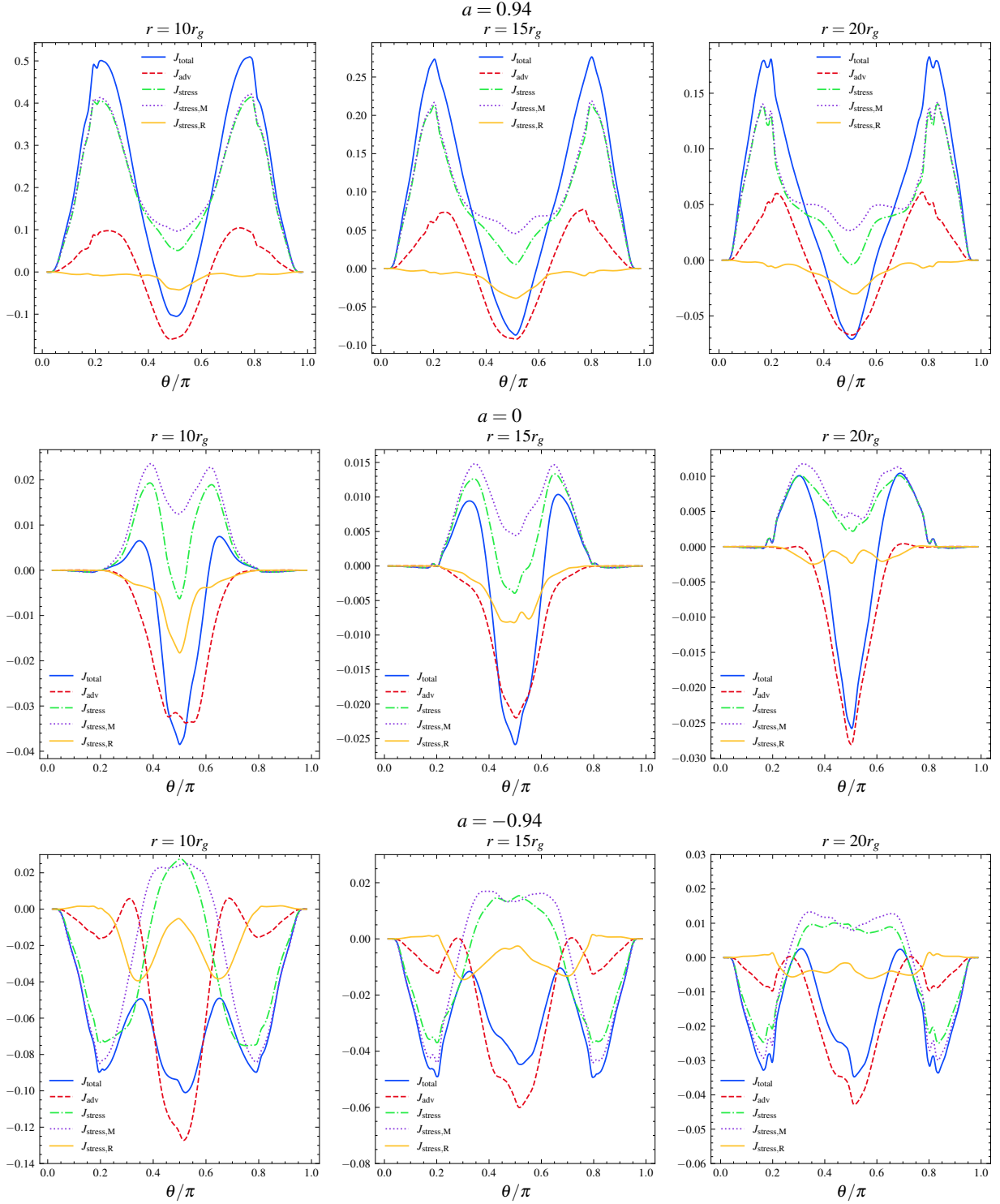


Figure 14. The radial angular momentum flux components \dot{J}^r as a function of the polar angle θ for a94b100 (top), a0b100 (middle) and aM94b100 (bottom) at 3 different radii, $r = 10, 15, 20r_g$.

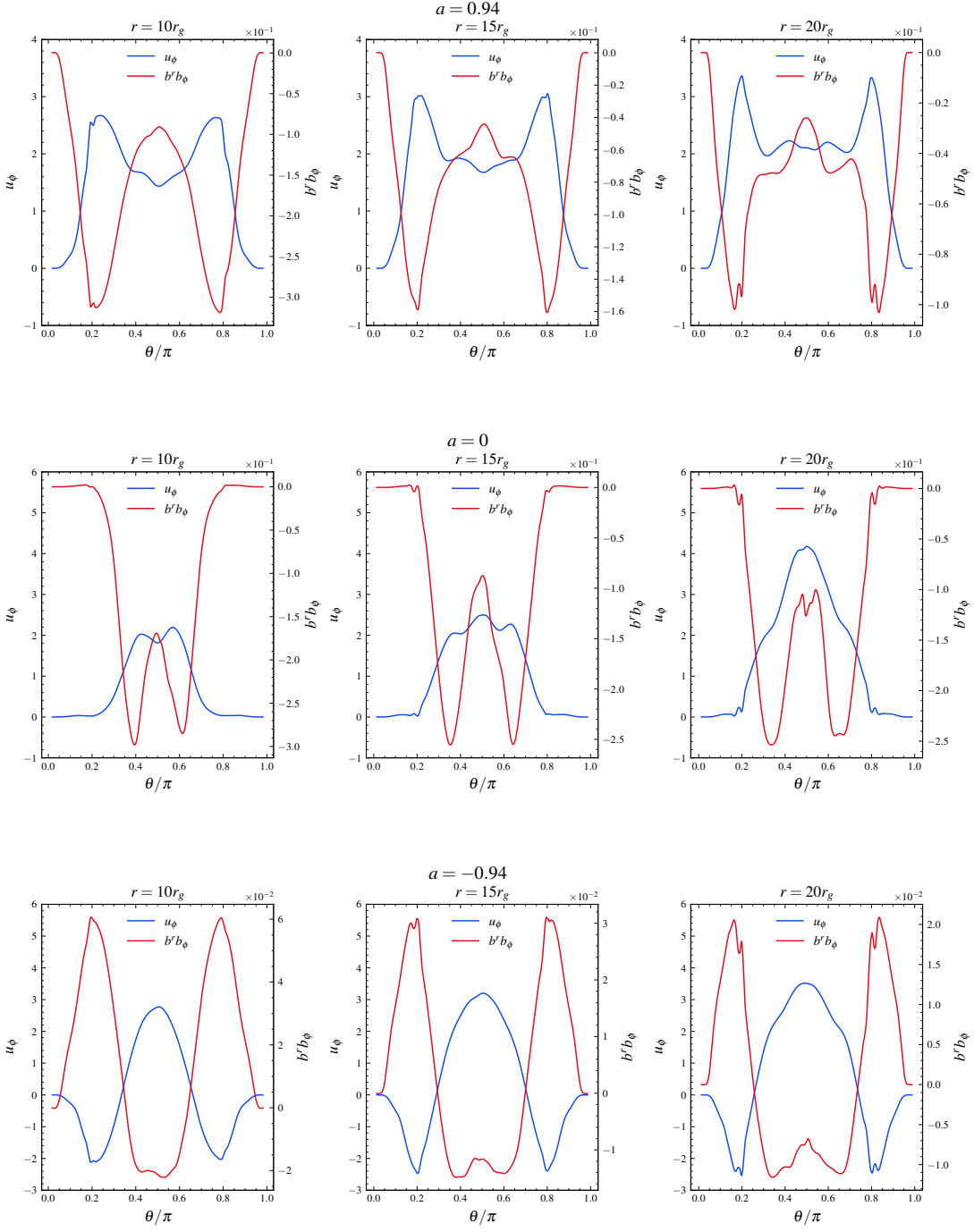


Figure 15. The toroidal component of the 4-velocity u^ϕ and $b^r b_\phi$ as a function of θ for a94b100 (top), a0b100 (middle) and aM94b100 (bottom), at the radii at which the radial angular momentum flux are obtained

Narayan et al. (2022), namely the MAD factor increases with spin until $a = 0.5$ after which it decreases. The fitting formula from Narayan et al. (2022), which we renormalized to account for the difference in definitions, accurately describes the distribution of Φ_B with spin. Therefore, this result holds across resolution, simulation duration and numerical method. The results of this analysis are summarized in the top row of Figure 4. We find

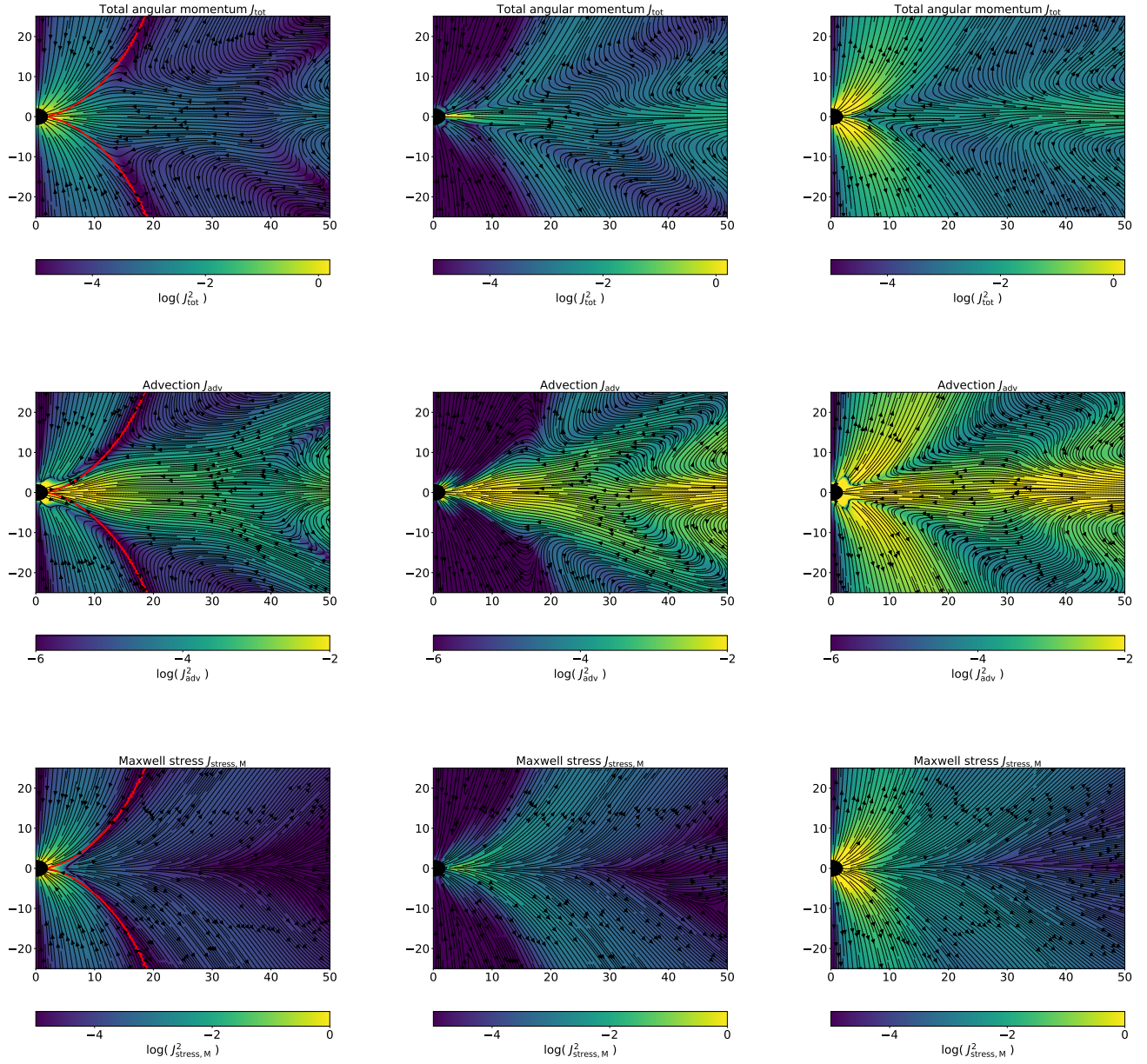


Figure 16. Time and ϕ -averaged maps of the angular momentum flux of the simulations with spin $a = -0.94$ (left), $a = 0$ (middle) and $a = 0.94$ (right). The color map represents the modulus of the angular momentum flux, $\sqrt{(\dot{J}^\theta)^2 + (\dot{J}^r)^2}$. The first row shows the total angular momentum flux, while the second and third rows show the contributions of the advection and Maxwell stress components, respectively. The color coding for each row is the same to ease the comparison. For $a = -0.94$, we use the red lines to denote the transition radius where the toroidal velocity component u^ϕ changes sign. It is seen that its position corresponds to the region in which the radial component of the Maxwell stress changes sign as well.

that the MAD parameter does not have a strong dependence on the initial magnetic field strength parameter β_0 . It only takes longer for the simulation to reach the MAD state, namely for the magnetic field to saturate to its final value. Once the MAD state is achieved, all simulations with different β_0 share the same characteristics, as shown in Figure 8.

6. We attempted to identify a characteristic variability time in the MAD regime by studying the temporal variation of Φ_B via the Fourier transform in Section 3.3. Contrary to the 2D case (see e.g. Chashkina et al. 2021), no clear period could be identified unambiguously. This is because in 3D simulation, accretion proceed via non-axisymmetric instabilities, such as the interchange instability (Spruit et al. 1995; McKinney et al. 2012; Begelman et al. 2022). Yet, the typical variability time we find is around a few hundreds t_g to a thousands, comparable to the estimates from Lloyd-Ronning et al. (2016) and James et al. (2022). This time scale is also comparable to the time scale inferred by Wong et al. (2021) who studied the layer between the disk and the jet.

Our results shed light on the differences in the accretion dynamics of disks in the MAD state across spins, prompting for more detailed analysis of the transport of angular momentum by jets and winds, as well as the the role of the toroidal magnetic field in (i) shaping the disk and jet and (ii) providing the norm of the MAD parameter, and via the norm understanding the efficiency of conversion between accretion luminosity and black hole spin energy deposited into the Poynting jets.

- 1 G.-Q. Zhang acknowledges support by the China Scholarship Council for 1 year study at Bar-Ilan University. DB and
 2 AP acknowledge support from the European Research Council via the ERC consolidating grant #773062 (acronym
 3 O.M.J.). B.-B.Z. acknowledges the support by the National Key Research and Development Programs of China
 4 (2022YFF0711404, 2022SKA0130102), the National SKA Program of China (2022SKA0130100), the National Natural
 5 Science Foundation of China (Grant Nos. 11833003, U2038105, U1831135, 12121003), the science research grants from
 6 the China Manned Space Project with NO.CMS-CSST-2021-B11, the Fundamental Research Funds for the Central
 7 Universities, the Program for Innovative Talents and Entrepreneur in Jiangsu. This work is performed on a HPC
 8 server equipped with 8 Nvidia DGX-V100 GPU modules at Nanjing University. We acknowledge the IT support from
 9 the computer lab of the School of Astronomy and Space Science at Nanjing University.

REFERENCES

- Abramowicz, M. A., Chen, X., Kato, S., Lasota, J.-P., & Regev, O. 1995, *ApJL*, 438, L37, doi: [10.1086/187709](https://doi.org/10.1086/187709)
- Anninos, P., Fragile, P. C., & Salmonson, J. D. 2005, *ApJ*, 635, 723, doi: [10.1086/497294](https://doi.org/10.1086/497294)
- Balbus, S. A., & Hawley, J. F. 1991a, *ApJ*, 376, 214, doi: [10.1086/170270](https://doi.org/10.1086/170270)
- . 1991b, *ApJ*, 376, 214, doi: [10.1086/170270](https://doi.org/10.1086/170270)
- . 1998a, *Reviews of Modern Physics*, 70, 1, doi: [10.1103/RevModPhys.70.1](https://doi.org/10.1103/RevModPhys.70.1)
- . 1998b, *Reviews of Modern Physics*, 70, 1, doi: [10.1103/RevModPhys.70.1](https://doi.org/10.1103/RevModPhys.70.1)
- Begelman, M. C., Scepi, N., & Dexter, J. 2022, *MNRAS*, 511, 2040, doi: [10.1093/mnras/stab3790](https://doi.org/10.1093/mnras/stab3790)
- Bégué, D., Pe'er, A., Zhang, G. Q., Zhang, B. B., & Pevzner, B. 2023, *ApJS*, 264, 32, doi: [10.3847/1538-4365/aca276](https://doi.org/10.3847/1538-4365/aca276)
- Bisnovatyi-Kogan, G. S., & Ruzmaikin, A. A. 1974, *Ap&SS*, 28, 45, doi: [10.1007/BF00642237](https://doi.org/10.1007/BF00642237)
- Blandford, R. D., & Znajek, R. L. 1977, *MNRAS*, 179, 433, doi: [10.1093/mnras/179.3.433](https://doi.org/10.1093/mnras/179.3.433)
- Chandra, M., Foucart, F., & Gammie, C. F. 2017, *ApJ*, 837, 92, doi: [10.3847/1538-4357/aa5f55](https://doi.org/10.3847/1538-4357/aa5f55)
- Chashkina, A., Bromberg, O., & Levinson, A. 2021, *MNRAS*, 508, 1241, doi: [10.1093/mnras/stab2513](https://doi.org/10.1093/mnras/stab2513)
- Chatterjee, K., & Narayan, R. 2022, *ApJ*, 941, 30, doi: [10.3847/1538-4357/ac9d97](https://doi.org/10.3847/1538-4357/ac9d97)
- Das, U., Begelman, M. C., & Lesur, G. 2018, *MNRAS*, 473, 2791, doi: [10.1093/mnras/stx2518](https://doi.org/10.1093/mnras/stx2518)
- De Villiers, J.-P., Hawley, J. F., & Krolik, J. H. 2003, *ApJ*, 599, 1238, doi: [10.1086/379509](https://doi.org/10.1086/379509)
- Dexter, J., Tchekhovskoy, A., Jiménez-Rosales, A., et al. 2020a, *MNRAS*, 497, 4999, doi: [10.1093/mnras/staa2288](https://doi.org/10.1093/mnras/staa2288)
- Dexter, J., Jiménez-Rosales, A., Ressler, S. M., et al. 2020b, *MNRAS*, 494, 4168, doi: [10.1093/mnras/staa922](https://doi.org/10.1093/mnras/staa922)
- Dihingia, I. K., Mizuno, Y., Fromm, C. M., & Rezzolla, L. 2023, *MNRAS*, 518, 405, doi: [10.1093/mnras/stac3165](https://doi.org/10.1093/mnras/stac3165)
- Event Horizon Telescope Collaboration, Akiyama, K., Alberdi, A., et al. 2019, *ApJL*, 875, L1, doi: [10.3847/2041-8213/ab0ec7](https://doi.org/10.3847/2041-8213/ab0ec7)

- Event Horizon Telescope Collaboration, Akiyama, K., Algaba, J. C., et al. 2021, *ApJL*, 910, L13, doi: [10.3847/2041-8213/abe4de](https://doi.org/10.3847/2041-8213/abe4de)
- Event Horizon Telescope Collaboration, Akiyama, K., Alberdi, A., et al. 2022a, *ApJL*, 930, L12, doi: [10.3847/2041-8213/ac6674](https://doi.org/10.3847/2041-8213/ac6674)
- . 2022b, *ApJL*, 930, L16, doi: [10.3847/2041-8213/ac6672](https://doi.org/10.3847/2041-8213/ac6672)
- Fishbone, L. G., & Moncrief, V. 1976, *ApJ*, 207, 962, doi: [10.1086/154565](https://doi.org/10.1086/154565)
- Font, J. A. 2008, *Living Reviews in Relativity*, 11, 7, doi: [10.12942/lrr-2008-7](https://doi.org/10.12942/lrr-2008-7)
- Gammie, C. F., McKinney, J. C., & Tóth, G. 2003, *ApJ*, 589, 444, doi: [10.1086/374594](https://doi.org/10.1086/374594)
- GRAVITY Collaboration, Abuter, R., Amorim, A., et al. 2018, *A&A*, 618, L10, doi: [10.1051/0004-6361/201834294](https://doi.org/10.1051/0004-6361/201834294)
- GRAVITY Collaboration, Bauböck, M., Dexter, J., et al. 2020, *A&A*, 635, A143, doi: [10.1051/0004-6361/201937233](https://doi.org/10.1051/0004-6361/201937233)
- Igumenshchev, I. V. 2008, *ApJ*, 677, 317, doi: [10.1086/529025](https://doi.org/10.1086/529025)
- James, B., Janiuk, A., & Nouri, F. H. 2022, *ApJ*, 935, 176, doi: [10.3847/1538-4357/ac81b7](https://doi.org/10.3847/1538-4357/ac81b7)
- Janiuk, A., & James, B. 2022, *A&A*, 668, A66, doi: [10.1051/0004-6361/202244196](https://doi.org/10.1051/0004-6361/202244196)
- Komissarov, S. S. 1999, *MNRAS*, 303, 343, doi: [10.1046/j.1365-8711.1999.02244.x](https://doi.org/10.1046/j.1365-8711.1999.02244.x)
- Liska, M., Tchekhovskoy, A., & Quataert, E. 2020, *MNRAS*, 494, 3656, doi: [10.1093/mnras/staa955](https://doi.org/10.1093/mnras/staa955)
- Liska, M. T. P., Chatterjee, K., Issa, D., et al. 2022, *ApJS*, 263, 26, doi: [10.3847/1538-4365/ac9966](https://doi.org/10.3847/1538-4365/ac9966)
- Lloyd-Ronning, N. M., Dolence, J. C., & Fryer, C. L. 2016, *MNRAS*, 461, 1045, doi: [10.1093/mnras/stw1366](https://doi.org/10.1093/mnras/stw1366)
- Marshall, M. D., Avara, M. J., & McKinney, J. C. 2018, *MNRAS*, 478, 1837, doi: [10.1093/mnras/sty1184](https://doi.org/10.1093/mnras/sty1184)
- Martí, J. M., & Müller, E. 2003, *Living Reviews in Relativity*, 6, 7, doi: [10.12942/lrr-2003-7](https://doi.org/10.12942/lrr-2003-7)
- McKinney, J. C., & Gammie, C. F. 2004, *ApJ*, 611, 977, doi: [10.1086/422244](https://doi.org/10.1086/422244)
- McKinney, J. C., Tchekhovskoy, A., & Blandford, R. D. 2012, *MNRAS*, 423, 3083, doi: [10.1111/j.1365-2966.2012.21074.x](https://doi.org/10.1111/j.1365-2966.2012.21074.x)
- Narayan, R., Chael, A., Chatterjee, K., Ricarte, A., & Curd, B. 2022, *MNRAS*, 511, 3795, doi: [10.1093/mnras/stac285](https://doi.org/10.1093/mnras/stac285)
- Narayan, R., Igumenshchev, I. V., & Abramowicz, M. A. 2003a, *PASJ*, 55, L69, doi: [10.1093/pasj/55.6.L69](https://doi.org/10.1093/pasj/55.6.L69)
- . 2003b, *PASJ*, 55, L69, doi: [10.1093/pasj/55.6.L69](https://doi.org/10.1093/pasj/55.6.L69)
- Narayan, R., Sądowski, A., Penna, R. F., & Kulkarni, A. K. 2012, *MNRAS*, 426, 3241, doi: [10.1111/j.1365-2966.2012.22002.x](https://doi.org/10.1111/j.1365-2966.2012.22002.x)
- Narayan, R., & Yi, I. 1994, *ApJL*, 428, L13, doi: [10.1086/187381](https://doi.org/10.1086/187381)
- . 1995, *ApJ*, 452, 710, doi: [10.1086/176343](https://doi.org/10.1086/176343)
- Noble, S. C., Gammie, C. F., McKinney, J. C., & Del Zanna, L. 2006, *ApJ*, 641, 626, doi: [10.1086/500349](https://doi.org/10.1086/500349)
- Novikov, I. D., & Thorne, K. S. 1973, in *Black Holes (Les Astres Occlus)*, 343–450
- Porth, O., Mizuno, Y., Younsi, Z., & Fromm, C. M. 2021a, *MNRAS*, 502, 2023, doi: [10.1093/mnras/stab163](https://doi.org/10.1093/mnras/stab163)
- . 2021b, *MNRAS*, 502, 2023, doi: [10.1093/mnras/stab163](https://doi.org/10.1093/mnras/stab163)
- Porth, O., Olivares, H., Mizuno, Y., et al. 2017, *Computational Astrophysics and Cosmology*, 4, 1, doi: [10.1186/s40668-017-0020-2](https://doi.org/10.1186/s40668-017-0020-2)
- Porth, O., Chatterjee, K., Narayan, R., et al. 2019, *ApJS*, 243, 26, doi: [10.3847/1538-4365/ab29fd](https://doi.org/10.3847/1538-4365/ab29fd)
- Rezzolla, L., & Zanotti, O. 2013, *Relativistic Hydrodynamics*
- Ripperda, B., Liska, M., Chatterjee, K., et al. 2022, *ApJL*, 924, L32, doi: [10.3847/2041-8213/ac46a1](https://doi.org/10.3847/2041-8213/ac46a1)
- Scepi, N., Dexter, J., & Begelman, M. C. 2022, *MNRAS*, 511, 3536, doi: [10.1093/mnras/stac337](https://doi.org/10.1093/mnras/stac337)
- Shakura, N. I., & Sunyaev, R. A. 1973, *A&A*, 24, 337
- Shankar, S., Mösta, P., Brandt, S. R., et al. 2022, *arXiv e-prints*, arXiv:2210.17509, doi: [10.48550/arXiv.2210.17509](https://doi.org/10.48550/arXiv.2210.17509)
- Sądowski, A., Narayan, R., Penna, R., & Zhu, Y. 2013, *MNRAS*, 436, 3856, doi: [10.1093/mnras/stt1881](https://doi.org/10.1093/mnras/stt1881)
- Spruit, H. C., Stehle, R., & Papaloizou, J. C. B. 1995, *MNRAS*, 275, 1223, doi: [10.1093/mnras/275.4.1223](https://doi.org/10.1093/mnras/275.4.1223)
- Stone, J. M., Gardiner, T. A., Teuben, P., Hawley, J. F., & Simon, J. B. 2008, *ApJS*, 178, 137, doi: [10.1086/588755](https://doi.org/10.1086/588755)
- Tchekhovskoy, A. 2019, *HARMPi: 3D massively parallel general relativistic MHD code*, *Astrophysics Source Code Library*, record ascl:1912.014. <http://ascl.net/1912.014>
- Tchekhovskoy, A., & McKinney, J. C. 2012, *MNRAS*, 423, L55, doi: [10.1111/j.1745-3933.2012.01256.x](https://doi.org/10.1111/j.1745-3933.2012.01256.x)
- Tchekhovskoy, A., Narayan, R., & McKinney, J. C. 2010, *ApJ*, 711, 50, doi: [10.1088/0004-637X/711/1/50](https://doi.org/10.1088/0004-637X/711/1/50)
- . 2011, *MNRAS*, 418, L79, doi: [10.1111/j.1745-3933.2011.01147.x](https://doi.org/10.1111/j.1745-3933.2011.01147.x)
- White, C. J., Quataert, E., & Gammie, C. F. 2020, *ApJ*, 891, 63, doi: [10.3847/1538-4357/ab718e](https://doi.org/10.3847/1538-4357/ab718e)
- White, C. J., Stone, J. M., & Quataert, E. 2019, *ApJ*, 874, 168, doi: [10.3847/1538-4357/ab0c0c](https://doi.org/10.3847/1538-4357/ab0c0c)
- Wong, G. N., Du, Y., Prather, B. S., & Gammie, C. F. 2021, *ApJ*, 914, 55, doi: [10.3847/1538-4357/abf8b8](https://doi.org/10.3847/1538-4357/abf8b8)
- Xie, F.-G., & Zdziarski, A. A. 2019, *ApJ*, 887, 167, doi: [10.3847/1538-4357/ab5848](https://doi.org/10.3847/1538-4357/ab5848)
- Yuan, F., Markoff, S., & Falcke, H. 2002, *A&A*, 383, 854, doi: [10.1051/0004-6361:20011709](https://doi.org/10.1051/0004-6361:20011709)

Yuan, F., & Narayan, R. 2014, *ARA&A*, 52, 529,
doi: [10.1146/annurev-astro-082812-141003](https://doi.org/10.1146/annurev-astro-082812-141003)

Yuan, F., Wang, H., & Yang, H. 2022, arXiv e-prints,
arXiv:2201.00512. <https://arxiv.org/abs/2201.00512>